

Vibration of solid and thin-walled slender structures made of soft materials by high-order beam finite elements

*Original*

Vibration of solid and thin-walled slender structures made of soft materials by high-order beam finite elements / Pagani, A.; Chiaia, P.; Carrera, E.. - In: INTERNATIONAL JOURNAL OF NON-LINEAR MECHANICS. - ISSN 0020-7462. - 160:(2024). [10.1016/j.ijnonlinmec.2023.104634]

*Availability:*

This version is available at: 11583/2985068 since: 2024-01-15T10:16:02Z

*Publisher:*

Elsevier Ltd

*Published*

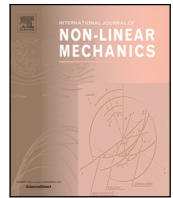
DOI:10.1016/j.ijnonlinmec.2023.104634

*Terms of use:*

This article is made available under terms and conditions as specified in the corresponding bibliographic description in the repository

*Publisher copyright*

(Article begins on next page)



# Vibration of solid and thin-walled slender structures made of soft materials by high-order beam finite elements

A. Pagani<sup>1,\*</sup>, P. Chiaia<sup>2</sup>, E. Carrera<sup>3</sup>

*Mul<sup>2</sup> Lab, Department of Mechanical and Aerospace Engineering Politecnico di Torino, 10129 Turin, Italy*

## ARTICLE INFO

### Keywords:

Hyperelasticity  
Unified formulation  
Nearly incompressible hyperelastic materials  
Natural frequencies  
Modal analysis

## ABSTRACT

In this work, high-order beam (1D) finite element models for the modal analysis of structures made of compressible and nearly-incompressible hyperelastic soft materials are presented in the well-established framework of Carrera Unified Formulation (CUF). In this investigation, the modal behavior of soft structures subjected to progressively increasing loads can be correctly predicted by higher-order structural theories, and the influence of pre-stress conditions applied on the modal response of structures is investigated. The mathematical formulation of hyperelastic isotropic materials is presented in terms of invariants of the right Cauchy–Green strain tensor, obtaining the most general expression of the Piola–Kirchhoff 2 stress tensor and tangent elasticity tensor, both independent of the model adopted for the material strain energy function. Governing equations in matrix forms for the static nonlinear analysis and subsequent vibration problem around non-trivial equilibrium states are derived through the Principle of Virtual Displacements (PVD) under a total Lagrangian formulation, defining the fundamental nuclei of stiffness matrices and internal and external forces vector, all independent of expansion theories and kinematic models adopted in the mathematical modeling of finite elements. Actual numerical results are obtained by an iterative Newton–Raphson linearized scheme coupled with line-search algorithms, and they are compared with results obtained by the commercial code ABAQUS. Our proposed models are tested with large strain problems involving hyperelastic slender and thin-walled structures, for which mode aberration such as crossing or bearing are observed.

## 1. Introduction

Large amplitude vibrations and nonlinear dynamics of complex structures are nowadays challenging research topics in different engineering fields; the dynamical behavior of membranes, soft actuators, sensors, and bio-inspired devices like micro-pumps and seismic isolators is fundamental for accurate structural modeling, health monitoring, and effective functionalities of smart devices. In this scenario, hyperelastic soft materials and structures have become more and more attractive due to their enhanced elastic properties and multi-physics applications since they show enhanced thermo-elastic or electro-elastic properties, and they have spread in manufacturing processes, smart material applications, design of micro and nano sensors, actuators, and bio-inspired structures also in critical environments. In the last decades, intense studies of hyperelastic material have been proposed, formulating the constitutive law in terms of a strain energy function approach based on different phenomenological capabilities shown by experimental testing of soft structures [1–4].

In hyperelasticity, large elastic deflections, strains, and rotations are observed when subjected to high static and cyclic loads. In early-stage research, these elastic properties of hyperelastic materials were investigated, typically adopting mathematical modeling in dynamical problems based on a-priori assumptions of the geometrical actual configuration, superimposing the deformed configurations and limiting the possible range of investigations. Lately, these limitations were overcome, and dynamical properties related to large strains were investigated, adopting extended mathematical formulations and experiments as done in [5,6]. In a finite element scenario, instead, dynamical problems involving soft materials and structures in the large amplitude regime deal with the time integration of governing equations strictly dependent on the viscoelastic constitutive behavior. Khaniki et al. [7] presents an intense review of the dynamics of hyperelastic soft structures. Due to both geometrical and material nonlinearities, including viscoelasticity, the strong nonlinear behavior of these materials results in a lack of analytical solutions available only for a

\* Corresponding author.

E-mail addresses: [alfonso.pagani@polito.it](mailto:alfonso.pagani@polito.it) (A. Pagani), [piero.chiaia@polito.it](mailto:piero.chiaia@polito.it) (P. Chiaia), [erasmo.carrera@polito.it](mailto:erasmo.carrera@polito.it) (E. Carrera).

<sup>1</sup> Associate Professor.

<sup>2</sup> PhD student.

<sup>3</sup> Professor of Aerospace Structures and Aeroelasticity.

few benchmark problems. In particular, the dynamic response of hyperelastic structures is governed by different structural features when near-resonance behavior is analyzed; the response is controlled by internal dissipation and viscoelasticity differently to cases far away from resonance where only mass and stiffness of the structures characterize the dynamical response, as reported by Amabili [8]. For these systems, softening and hardening behavior are often observed; thus, the frequency response can be characterized by complex phenomena and internal resonance. Pamplona et al. [9] analyzed the internal resonance behavior of thin-walled cylindrical vessels under internal pressure. Breslavsky et al. [10] investigated the large amplitude vibration of thin plates adopting a Neo-Hookean strain energy function hyperelastic model. The nonlinear vibrations of thin hyperelastic plates were also investigated by the same authors in [11]. Soares et al. [12] analyzed the nonlinear vibration of thin hyperelastic membranes in pre-stressed configurations. Balasubramanian et al. [13] presented an experimental and numerical investigation of vibrations of clamped rubber plates. Arani et al. [14] analyzed the dynamic response of an incompressible hyperelastic cylindrical shell subjected to radial harmonic perturbations.

Despite these difficulties, small-amplitude vibrations and modal analysis of beams, plates, and shells hyperelastic structures are interesting fields thanks to their application. Natural frequencies and mode shapes of hyperelastic media in the compressible and nearly-incompressible material regimes are the starting point for a complete description of a full dynamic response characterization. Thanks to their huge elastic properties, typical investigations of modal behavior of soft structures are investigated in pre-stressed conditions; the influence of stretching ratios and large strains or rotations on the natural frequencies and mode shapes is an attractive research field, but also, in this case, available solutions refer to simple geometries or boundary conditions considered.

In this work, a finite element formulation of beam-like structures based on CUF for the modal analysis of isotropic hyperelastic materials is proposed. In the proposed finite element model, the displacement field is expressed by kinematic models and expansion theories coupled under a recursive index notation. Refined fully nonlinear structural models are defined in CUF formalism, which allows a straightforward implementation of any higher-order model and compact definitions of matrix-form physical quantities independent of the polynomial expansion adopted [15–17]. The capabilities of 1D beam and 2D plate models in modal analysis of materials and structures in non-trivial equilibrium states are established in [18,19]. More recently, Unified models have been extended to hyperelastic materials finite element modeling, and the capabilities of beam, plates, and solid models to deal with static nonlinear analysis of soft compressible and nearly-incompressible soft structures are established in [20–22].

Here, the fully nonlinear 1D beam model for the modal analysis of hyperelastic materials and structures is presented, defining the finite element procedure in the CUF framework: (i) first, the analytic expression of physical quantities (Piola–Kirchhoff 2 stress tensor, tangent elasticity tensor) under the hyperelastic constitutive law are derived, written in terms of invariant of the right Cauchy–Green strain tensor, in Section 2; (ii) second, Unified 1D beam models, kinematic models and cross-section expansion theories are described in Section 3; (iii) subsequently, the nonlinear governing equations for the nonlinear static analysis and linear free vibration problem in non-trivial equilibrium states are exploited through the Principle of Virtual Displacements, defining the matrix-form and Fundamental Nuclei (FN) of internal and external forces vector, tangent stiffness matrix and mass matrix, presented in Section 4; (iv) actual numerical results and analysis of different benchmark problems through refined 1D models are discussed in Section 5, presenting the accuracy of our models in the analysis of compressible and nearly-incompressible structures; (v) finally, the main conclusions evinced are discussed in Section 6.

## 2. Constitutive law

### 2.1. Kinematics and strain measures

Let  $\Omega$  be a continuum body in the Euclidean space and let  $\Sigma = \{\mathbf{e}_1, \mathbf{e}_2, \mathbf{e}_3\}$  be the classical Cartesian reference frame. A material particle  $\mathbf{P}_0 = (x^0, y^0, z^0)$  follows the evolution in time of the continuum body that occupies a continuous sequence of regions of the Euclidean space. Starting from the *reference* configuration  $\Omega_0$ , the configuration at the generic instant  $t$  is called the *current configuration*, and the material particle now occupies the position  $\mathbf{P} = (x, y, z)$ . In the classical continuum mechanics approach, the current position of the generic material point is described by the *deformation function*, which maps the material point in the actual configuration to the related position in the reference configuration. Thereafter, one can define the classical strain measures adopted in continuum mechanics, namely the deformation gradient  $\mathbf{F} = \partial\mathbf{P}/\partial\mathbf{P}_0$  and the right Cauchy–Green strain tensor  $\mathbf{C} = \mathbf{F}^T\mathbf{F}$ . Typically, isotropic hyperelastic mathematical models are defined starting from the invariants of the right Cauchy–Green strain tensor, following objectivity arguments and independence with respect to the reference frame, thus one defines:

$$I_1 = \text{tr}(\mathbf{C}) \quad (1)$$

$$I_2 = \frac{1}{2}((\text{tr}(\mathbf{C}))^2 - \text{tr}(\mathbf{C}^2)) = \text{tr}(\text{cof}(\mathbf{C})) \quad (2)$$

$$I_3 = \det(\mathbf{C}) = \det(\mathbf{F}^T\mathbf{F}) = J^2 \quad (3)$$

where  $\text{tr}(\cdot)$  and  $\det(\cdot)$  are the trace and the determinant operators,  $\text{cof}(\cdot)$  is the matrix of the cofactors and  $J$  is the determinant of the deformation gradient tensor. Different strain measures will be assumed in this work; the Green–Lagrange strain tensor is also here presented. Analyzing the infinitesimal behavior of a material fiber during the evolution process of the body to its deformed state, one can define the Green–Lagrange strain tensor starting from the right Cauchy–Green tensor, obtaining the following relation:

$$\mathbf{E} = \frac{1}{2}(\mathbf{F}^T\mathbf{F} - \mathbf{I}) = \frac{1}{2}(\mathbf{C} - \mathbf{I}) \quad (4)$$

### 2.2. Hyperelastic constitutive law in terms of invariants

In the present work, hyperelastic models are defined under the so-called decoupled formulation in accordance with the Flory decomposition [23] by considering the deformation gradient as the product of its *volumetric* and *isochoric* components, thus:

$$\mathbf{F} = \mathbf{F}_{vol}\bar{\mathbf{F}} \rightarrow \mathbf{F}_{vol} = J^{\frac{1}{3}}\mathbf{I}; \quad \bar{\mathbf{F}} = J^{-\frac{1}{3}}\mathbf{F} \quad (5)$$

Consistently with the decomposition here adopted, also the right Cauchy–Green tensor is rewritten as:

$$\mathbf{C} = \mathbf{C}_{vol}\bar{\mathbf{C}} \rightarrow \mathbf{C}_{vol} = J^{\frac{2}{3}}\mathbf{I}; \quad \bar{\mathbf{C}} = J^{-\frac{2}{3}}\mathbf{C} \quad (6)$$

In the above relations,  $\mathbf{F}_{vol}$ ,  $\mathbf{C}_{vol}$  are associated to a *volume-changing* behavior, instead  $\bar{\mathbf{F}}$ ,  $\bar{\mathbf{C}}$  to a *volume-preserving* behavior. In the principal reference frame of the eigenvector of each tensor, one can define then the so-called *modified principal stretches* as the eigenvalues of  $\bar{\mathbf{F}}$ ,  $\bar{\mathbf{C}}$ .

In this framework then, the strain–energy function is assumed as a *decoupled* representation, in which the volumetric and isochoric parts are two distinct contributions:

$$\Psi(\mathbf{C}) = \Psi_{vol}(J) + \Psi_{iso}(\bar{\mathbf{C}}) = U(J) + \bar{\Psi}(\bar{I}_1, \bar{I}_2) \quad (7)$$

where  $\bar{I}_1$ ,  $\bar{I}_2$  are the invariants of the isochoric part of the right Cauchy–Green tensor  $\bar{\mathbf{C}}$ . In Eq. (7), the volumetric part of the strain energy function is considered a penalization function to enforce material incompressibility. In literature, many models for  $U(J)$  are described. In

the present paper, the classical quadratic volumetric expression of  $U(J)$ , presented by Sussman and Bathe [24], is adopted, explicitly:

$$U(J) = \frac{1}{D_1} (J - 1)^2 = \frac{k}{2} (J - 1)^2 \quad (8)$$

where  $D_1 = 2/k$  is the incompressibility parameter defined starting from the bulk modulus  $k$  of the material. Consistently, with the previously introduced decomposition, the PK2 (Piola–Kirchhoff 2) is written as sum of *volume-changing* and *volume-preserving* parts:

$$\mathbf{S} = 2 \frac{\partial \Psi}{\partial \mathbf{C}} = \mathbf{S}_{vol} + \mathbf{S}_{iso} \quad (9)$$

$$\mathbf{S}_{vol} = 2 \frac{\partial \Psi_{vol}}{\partial \mathbf{C}} = J^{-1} p \mathbf{C}^{-1} \quad (10)$$

$$\mathbf{S}_{iso} = 2 \frac{\partial \tilde{\Psi}}{\partial \mathbf{C}} = J^{-\frac{2}{3}} \left( \mathbb{I} - \frac{1}{3} \mathbf{C}^{-1} \otimes \mathbf{C} \right) : \tilde{\mathbf{S}} = J^{-\frac{2}{3}} \mathbb{P} : \tilde{\mathbf{S}} \quad (11)$$

where  $\mathbb{P}$  is the fourth-order projection tensor, required in the definition of the correct deviatoric operator in the material reference frame due to the Total Lagrangian Formulation,  $\tilde{\mathbf{S}} = \frac{\partial \tilde{\Psi}}{\partial \mathbf{C}}$  is the rescaled/modified PK2 stress tensor and  $\mathbb{I} = \delta_{ik} \delta_{jl} \mathbf{e}_i \otimes \mathbf{e}_j \otimes \mathbf{e}_k \otimes \mathbf{e}_l$  is the fourth-order identity tensor. In this explicit form, the *hydrostatic pressure*  $p$  in Eq. (11) is a crucial variable in the stress description of nearly-incompressible material. Under the hypothesis of volumetric strain energy function Eq. (8), the hydrostatic pressure is related to the total volumetric strain by a linear relation, in fact:

$$p = \frac{\partial \Psi_{vol}}{\partial J} = \frac{\partial}{\partial J} \left( \frac{k}{2} (J - 1)^2 \right) = k(J - 1) = k \left( \frac{\Omega}{\Omega_0} - 1 \right) = k \left( \frac{\Delta \Omega}{\Omega_0} \right) = k \varepsilon_v$$

This derivation holds independently on the specific strain energy function considered, but a linear relation between the hydrostatic pressure and the volumetric strain is found only under the hypothesis of the classical quadratic volumetric model. To stabilize these formulations, different volumetric models have been presented in the last decade to alleviate the volumetric locking arising from this limitation [25]. In the framework of decoupled hyperelastic models, the hydrostatic pressure is used as penalization of Lagrange's multiplier to enforce incompressibility (namely  $J = 1$ ).

### 2.3. Incremental formulation and tangent elasticity tensor

In the framework of the finite element method for geometrically and materially nonlinear problems, incremental formulations are typically employed. In a common hyperelastic scenario, the constitutive equation Eq. (9) can be rewritten by the total differential form [26]:

$$\Delta \mathbf{S} = \mathbb{C} \frac{1}{2} \Delta \mathbf{C} = \mathbb{C} \Delta \mathbf{E} \quad (12)$$

where  $\mathbb{C}$  is the so-called *tangent elasticity tensor*, defined starting the linearization of the constitutive law:

$$\mathbb{C} = 2 \frac{\partial \mathbf{S}(\mathbf{C})}{\partial \mathbf{C}} = 4 \frac{\partial^2 \Psi}{\partial \mathbf{C} \partial \mathbf{C}} \quad (13)$$

The previously introduced decomposition of volume-changing and volume-preserving components is also considered for the tangent elasticity tensor:

$$\mathbb{C} = \mathbb{C}_{vol} + \mathbb{C}_{iso} \quad (14)$$

These components can be derived straightforwardly, starting from the definition of PK2 and applying the derivative operator with respect to the right Cauchy–Green strain tensor:

$$\mathbb{C}_{vol} = J(p + J \frac{dp}{dJ}) \mathbf{C}^{-1} \otimes \mathbf{C}^{-1} - 2Jp \mathbf{C}^{-1} \odot \mathbf{C}^{-1} \quad (15)$$

$$\mathbb{C}_{iso} = 2(\mathbb{P} : \tilde{\mathbf{S}}) \otimes \frac{\partial J^{-2/3}}{\partial \mathbf{C}} + 2J^{-2/3} \frac{\partial (\mathbb{P} : \tilde{\mathbf{S}})}{\partial \mathbf{C}} \quad (16)$$

where  $\mathbb{I} = \delta_{il} \delta_{jk} \mathbf{e}_i \otimes \mathbf{e}_j \otimes \mathbf{e}_k \otimes \mathbf{e}_l$ ,  $\mathbf{S} = (\mathbb{I} + \mathbb{I})/2$  is fourth-order unit tensor and  $\mathbf{C}^{-1} \odot \mathbf{C}^{-1}$  is the symmetric part of the Hadamard product between  $\mathbf{C}^{-1}$  and  $\mathbf{C}^{-1}$ . Here, only the analytic expression of these components is reported, but more details about the derivation can be found in [26].

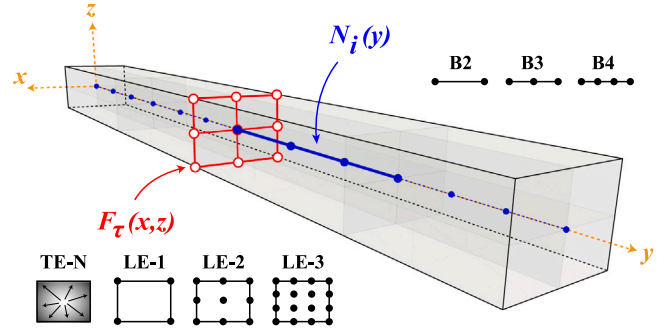


Fig. 1. Unified 1D models: scheme and kinematic models coupling representation.

### 3. Unified formulation of hyperelastic beams

The extension of CUF finite element models for hyperelastic materials has already been presented by Pagani et al. [20], in which the formulation of hyperelastic solid beam finite elements in the CUF framework is established. Lately, Augello et al. [21] and Pagani et al. [22] presented the unified 2D plate and 3D solid hexahedral models for hyperelastic materials assessing the capabilities of CUF models by different benchmark problems in compressible and nearly-incompressible hyperelasticity. Under CUF formalism, the unknown displacement field is expressed as a polynomial expansion of the discretized unknown displacement variables, adopting a recursive index notation, that allows the coupling of kinematic models and arbitrary cross-section expansion functions. In the classical orthonormal  $\{x, y, z\}$  Cartesian reference frame, the three-dimensional displacement field is then expressed as

$$\mathbf{u}(x, y, z) = F_r(x, z) \mathbf{u}_r(y) \quad \tau = 1, \dots, M \quad (17)$$

where  $F_r(x, z)$  is the set of cross-section expansion functions that characterizes the expansion theory in the mathematical model adopted,  $M$  is the cross-section expansion order and  $\mathbf{u}_r$  is the vector of generalized displacement components along the beam axis. Fig. 1 shows the geometrical representation of the unified 1D beam CUF model.

In the previous definition of displacement field Eq. (17), Einstein's notation for repeated indices is employed. Higher-order structural theories can be implemented by choosing the expansion basis function  $F_r(x, z)$  that completely characterizes the model. In the present work, two different classes of expansion functions are considered, TE (Taylor Expansion) class and LE (Lagrange Expansion) class. TE models make use of 2D MacLaurin polynomials as the basis for the cross-section expansion of the generalized beam axis displacements and, depending on the expansion order, higher-order theories are defined hierarchically in an automatic way. As examples, the TE-1 linear expansion model is explicitly expressed as

$$\begin{cases} u_x(x, y, z) = u_{x1}(y) + xu_{x2}(y) + zu_{x3}(y) \\ u_y(x, y, z) = u_{y1}(y) + xu_{y2}(y) + zu_{y3}(y) \\ u_z(x, y, z) = u_{z1}(y) + xu_{z2}(y) + zu_{z3}(y) \end{cases} \quad (18)$$

where  $u_{x_i}$ ,  $u_{y_i}$  and  $u_{z_i}$ ,  $i = 1 \dots 3$ , stand for the displacements and rotation components of the beam axis, and the TE-2 parabolic expansion models expressed as

$$\begin{cases} u_x(x, y, z) = u_{x1}(y) + xu_{x2}(y) + zu_{x3}(y) + x^2u_{x4}(y) + xzu_{x5}(y) + z^2u_{x6}(y) \\ u_y(x, y, z) = u_{y1}(y) + xu_{y2}(y) + zu_{y3}(y) + x^2u_{y4}(y) + xzu_{y5}(y) + z^2u_{y6}(y) \\ u_z(x, y, z) = u_{z1}(y) + xu_{z2}(y) + zu_{z3}(y) + x^2u_{z4}(y) + xzu_{z5}(y) + z^2u_{z6}(y) \end{cases} \quad (19)$$

where, again,  $u_{x_i}$ ,  $u_{y_i}$  and  $u_{z_i}$ ,  $i = 1 \dots 6$ , are the generalized unknowns of the problem, referred to the reference beam axis considered. In the

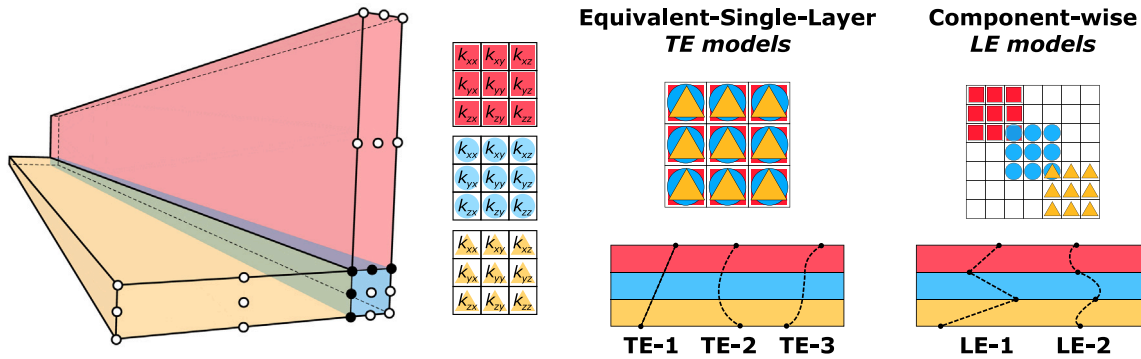


Fig. 2. Unified 1D models: Equivalent-single-layer and component-wise models.

case of LE-models, instead, along the beam cross-section, Lagrange-type polynomials are adopted as expansion basis in a resulting model of pure displacement variables exploiting the isoparametric formulation. In the present work, the linear LE-2 (four-node), parabolic LE-3 (nine-node), and cubic LE-4 (sixteen-node) expansion models will be adopted in the formulation of the cross-section kinematics. As examples, the displacement field of a LE-2 parabolic expansion model is reported, expressed as

$$\begin{cases} u_x(x, y, z) = F_1(x, z)u_{x_1}(y) + F_2(x, z)u_{x_2}(y) + F_3(x, z)u_{x_3}(y) \\ \quad + \dots + F_9(x, z)u_{x_9}(y) \\ u_y(x, y, z) = F_1(x, z)u_{y_1}(y) + F_2(x, z)u_{y_2}(y) + F_3(x, z)u_{y_3}(y) \\ \quad + \dots + F_9(x, z)u_{y_9}(y) \\ u_z(x, y, z) = F_1(x, z)u_{z_1}(y) + F_2(x, z)u_{z_2}(y) + F_3(x, z)u_{z_3}(y) \\ \quad + \dots + F_9(x, z)u_{z_9}(y) \end{cases} \quad (20)$$

where the cross-section expansion functions are the classical Lagrange polynomials in the parabolic case. One key feature of LE expansion models is the local expansion of the specific zone of the cross-section by pure unknowns of the model, guaranteeing local refinements. A more detailed derivation of LE-class models and basis function adopted can be found in [27]. The capabilities of higher-order TE and LE models to deal with the component-wise modeling of mechanical and aeronautical structures, the nonlinear static analysis, and pre-stressed vibration analysis are demonstrated in [28–30]. Finally, independently of the structural expansion theory adopted, the generalized displacement field along the beam axis (chosen as reference for the cross-section expansion) is discretized following the classical finite element procedures, thus

$$\mathbf{u}_\tau(y) = N_i(y)\mathbf{u}_{\tau i} \quad (21)$$

where the generalized nodal displacements along the beam axis are now expanded adopting the  $N_i(y)$  shape functions, obtaining the final resulting discretized unknown of the problem  $\mathbf{u}_{\tau i}$ . In Eq. (21), the index  $i$  stand for the summation along the finite nodes per element adopted in the discretization of the beam axis, and  $N_n$  stand for the order of the expansion that, in the case of classical Lagrange's shape function involved in FEM (and also adopted in this present work), corresponds with the total number of finite nodes. Finally, the 3-D displacement field is expressed, in the CUF framework as

$$\mathbf{u}(x, y, z) = F_\tau(x, z)\mathbf{u}_\tau(y) = F_\tau(x, z)N_i(y)\mathbf{u}_{\tau i} \quad (22)$$

Eq. (22) is the most general expression of displacement field approximated with a coupled expansion of cross-section structural theories and finite element approximation, in a resulting final formulation of refined higher-order 1D beam theories independent of the chosen kinematic models of expansion theory adopted. In this work, both TE-class models and LE-class models are adopted. In literature, the adoption of these different models results in different approximation theories of the displacement and stress field inside the structure. The

TE-class models are addressed as ESLMs (Equivalent Single Layer Models), in which the displacement field of the beam cross-section is evaluated as an *homogenized* equivalent cross-section in which the properties of the material are combined to build an equivalent but unique description. From a finite element matrices point of view, the properties of each layer in terms of stiffness matrices are summed together in a resulting single layer in which the properties of the entire cross-section are included. The LE-class models are addressed as Layer-Wise (LW) or Component-Wise (CW) theories and they are typically adopted in composite materials modeling [31,32]; they allow an independent kinematic description of each cross-section combining the mechanical properties of different cross-section sub-components at their interfaces, by imposing displacement continuity in the case of node superposition since the degrees of freedom are pure nodal displacement components. The difference between these models and assembling procedures are shown in Fig. 2. Typically, LW models lead to a more accurate description of both displacement components and stress fields since ESLMs show limitation in the computation of out-of-plane normal and transverse shear. Commonly adopted beam models, based on a polynomial expansion of the displacement field, are typically inaccurate in the geometrically and material nonlinear analysis due to a-priori assumption of displacement components that lead to incorrect stresses distribution, such as transverse normal and shear stresses at the beam edges. In the framework of CUF, as detailed and analyzed in Carrera et al. [33], the adoption of higher-order models implemented straightforwardly in a finite element scenario can deal efficiently with this inconsistency, providing accurate stress distributions considering enriched displacement field kinematics and avoiding the adoption of ad-hoc technique such as shear correction factors or warping functions.

#### 4. Governing equations in terms of Fundamental Nuclei

##### 4.1. Internal, external and inertial forces vectors

In the present work, the derivation of the governing equation in weak form is carried out by means of PVD. Supposing that the body volume forces are negligible, PVD is written as:

$$\delta \mathcal{L}_{int} + \delta \mathcal{L}_{ine} = \delta \mathcal{L}_{ext} \quad (23)$$

where  $\delta \mathcal{L}_{int}$  is the internal strain energy done by virtual displacement,  $\mathcal{L}_{ext}$  is the work of external loads done by virtual displacements and  $\mathcal{L}_{ine}$  is the work done by inertia forces, defined as:

$$\begin{aligned} (a) \quad \delta \mathcal{L}_{int} &= \int_{\Omega} \delta \mathbf{E}^T \mathbf{S} dV & (b) \quad \delta \mathcal{L}_{ext} &= \int_{\Omega} \delta \mathbf{u}^T \mathbf{p} dV \\ (c) \quad \delta \mathcal{L}_{ine} &= \int_{\Omega} \delta \mathbf{u}^T \rho \ddot{\mathbf{u}} dV \end{aligned} \quad (24)$$

where  $\mathbf{S}$  is the PK2 stress tensor,  $\mathbf{E}$  is the Green–Lagrange strain tensor,  $\mathbf{p}$  is the vector of external loads,  $\ddot{\mathbf{u}}$  is the nodal accelerations vector and all volume integrals are referred to the material (or reference)



configuration. These energetic contributions, under the CUF formalism, can be written in matrix form in terms of FNs (Fundamental Nuclei) by imposing the discretization adopted for the displacement field of the single refined finite element model. To define the matrix form of these energetic contributions, the virtual variation of the displacement field is introduced, adopting the same index notation and polynomial expansion with different independent indices, adopting the  $j$  index for virtual measures along the axis nodes and  $s$  index for the cross-section expansion of virtual displacement component, obtaining an independent quantity with respect of real one, therefore:

$$\delta \mathbf{u}(x, y, z) = F_s(x, z) \delta \mathbf{u}_s(y) = F_s(x, z) N_j(y) \delta \mathbf{u}_{sj} \quad j = 1, 2, \dots, N_n, \\ s = 1, \dots, M \quad (25)$$

Referring to the internal energy contribution, the full Green–Lagrange strain tensor can be rewritten in terms of nodal displacement unknowns and expansion functions with the same index notation. Introducing now *Voigt's notation* for the representation of physical symmetric quantities, the strain tensor is written in vector form:

$$\mathbf{E} = (\mathbf{b}_l + \mathbf{b}_{nl}) \mathbf{u} = (\mathbf{b}_l + \mathbf{b}_{nl}) F_\tau(x, z) N_i(y) \mathbf{u}_{\tau i} = (\mathbf{B}_l^{\tau i} + \mathbf{B}_{nl}^{\tau i}) \mathbf{u}_{\tau i} \quad (26)$$

Applying the formal matrices of derivatives operators to expansion function of the displacement field, the expressions of algebraic matrices  $\mathbf{B}_l^{\tau i}$  and  $\mathbf{B}_{nl}^{\tau i}$  are carried out, and their explicit forms can be found in Pagani et al. [28]. Under these assumptions, the virtual variation of the strain tensor is:

$$\delta \mathbf{E} = \delta((\mathbf{B}_l^{\tau i} + \mathbf{B}_{nl}^{\tau i}) \mathbf{u}_{\tau i}) = (\mathbf{B}_l^{sj} + 2\mathbf{B}_{nl}^{sj}) \delta \mathbf{u}_{sj} \quad (27)$$

Substituting now Eq. (27) into Eq. (24)(a):

$$\delta \mathcal{L}_{int} = \int_{\Omega} \delta \mathbf{u}_{sj}^T (\mathbf{B}_l^{sj} + 2\mathbf{B}_{nl}^{sj})^T \mathbf{S} dV = \delta \mathbf{u}_{sj}^T \left[ \int_{\Omega} (\mathbf{B}_l^{sj} + 2\mathbf{B}_{nl}^{sj})^T \mathbf{S} dV \right] = \delta \mathbf{u}_{sj}^T \mathbf{F}_{int}^{sj} \quad (28)$$

where  $\mathbf{F}_{int}^{sj}$  the  $3 \times 1$  FN of the internal forces vector:

$$\mathbf{F}_{int}^{sj} = \int_{\Omega} (\mathbf{B}_l^{sj} + 2\mathbf{B}_{nl}^{sj})^T \mathbf{S} dV \quad (29)$$

Referring to the external load contribution in the variational principle, the FN of the external load vector is exploited by means of the same derivation procedure described for the internal energy contribution. If  $\mathbf{p}$  is the conservative loads vector applied to the structure, one has:

$$\delta \mathcal{L}_{ext} = \int_{\Omega} \delta \mathbf{u}^T \mathbf{p} dV = \int_{\Omega} \delta \mathbf{u}_{sj}^T F_s(x, z) N_j(y) \mathbf{p} dV = \delta \mathbf{u}_{sj}^T \mathbf{F}_{ext}^{sj} \quad (30)$$

where  $\mathbf{F}_{ext}^{sj}$  the  $3 \times 1$  FN of the external forces vector:

$$\mathbf{F}_{ext}^{sj} = \int_{\Omega} F_s(x, z) N_j(y) \mathbf{p} dV \quad (31)$$

Regarding the inertial contribution of the energetic balance principle, one can write, following the same derivation procedure, the matrix form of the inertial energy contribution:

$$\delta \mathcal{L}_{ine} = \int_{\Omega} \delta \mathbf{u}^T \rho \ddot{\mathbf{u}} dV = \int_{\Omega} \delta \mathbf{u}_{sj}^T F_s(x, z) N_j(y) \rho F_\tau(x, z) N_i(y) \ddot{\mathbf{u}}_{\tau i} dV \\ = \delta \mathbf{u}_{sj}^T \mathbf{M}^{\tau sij} \ddot{\mathbf{u}}_{\tau i} \quad (32)$$

where  $\mathbf{M}^{\tau sij}$  the  $3 \times 3$  FN of the mass matrix:

$$\mathbf{M}^{\tau sij} = \int_{\Omega} F_s(x, z) N_j(y) \rho \mathbf{I} F_\tau(x, z) N_i(y) dV \quad (33)$$

Adopting CUF, all these FNs result independent of the polynomial expansion order; thus, Eqs. (29), (30), and (33) define unique expressions of physical quantities for any arbitrarily polynomial expansion. Assigning the kinematic models for the beam axis discretization and the cross-section expansion basis functions, so by choosing the shape functions  $N_i(y)$ ,  $N_j(y)$ ,  $F_\tau(x, z)$  and  $F_s(x, z)$  and exploiting the summation over the recursive indices expansion (namely the summation

over indices  $i$  and  $j$ ,  $\tau$  and  $s$ ), FN are obtained straightforwardly. More details about the generic expansion of the FN can be found in [34].

Considering then Eqs. (28), (30) and (32), the variational principle written in matrix form is:

$$\delta \mathbf{u}_{sj}^T \mathbf{F}_{int}^{sj} + \delta \mathbf{u}_{sj}^T \mathbf{M}^{\tau sij} \ddot{\mathbf{u}}_{\tau i} = \delta \mathbf{u}_{sj}^T \mathbf{F}_{ext}^{sj} \quad (34)$$

The summation over indices  $\tau$ ,  $s$ ,  $i$  and  $j$  gives the internal and external forces vectors and the mass matrix for the single element considered, obtained straightforwardly by following the CUF assembling procedure [34]. Assembling the FE matrices along the discretization considered, the final definition of PVD in matrix form states:

$$\mathbf{F}_{int}(\mathbf{u}) + \mathbf{M}\ddot{\mathbf{u}} = \mathbf{F}_{ext}(\mathbf{f}) \quad (35)$$

#### 4.2. Linearization of governing equations

Governing equations for the undamped vibration problem in non-trivial equilibrium states, based on the PVD, are carried out here. In hyperelasticity, the presence of both geometrical and physical nonlinearities in the constitutive equation leads to strongly nonlinear governing equilibrium equations. In a finite element scenario, solutions are typically obtained by numerical incremental-iterative schemes based on linearization principles. Starting from Eq. (35), the *unbalanced nodal forces vector* or residual nodal forces vector is defined as:

$$\boldsymbol{\phi}_{res}(\mathbf{u}, \ddot{\mathbf{u}}, \mathbf{f}) = \mathbf{F}_{int} + \mathbf{M}\ddot{\mathbf{u}} - \mathbf{F}_{ext} \quad (36)$$

In this way, the generic equilibrium condition is equivalently expressed by the condition  $\boldsymbol{\phi}_{res}(\mathbf{u}, \ddot{\mathbf{u}}, \mathbf{f}) = 0$ . If  $(\mathbf{u}_0, \ddot{\mathbf{u}}_0, \mathbf{f}_0)$  is the given equilibrium state, one can linearize Eq. (36) considering a Taylor expansion of the residual nodal forces vector truncated at first order for an increment  $(\Delta \mathbf{u}, \Delta \ddot{\mathbf{u}}, \Delta \mathbf{f})$ , thus

$$\boldsymbol{\phi}_{res}(\mathbf{u}_0 + \Delta \mathbf{u}, \ddot{\mathbf{u}}_0 + \Delta \ddot{\mathbf{u}}, \mathbf{f}_0 + \Delta \mathbf{f}) = \boldsymbol{\phi}_{res}(\mathbf{u}_0, \ddot{\mathbf{u}}_0, \mathbf{f}_0) + \frac{\partial \boldsymbol{\phi}_{res}}{\partial \mathbf{u}} \Delta \mathbf{u} + \frac{\partial \boldsymbol{\phi}_{res}}{\partial \ddot{\mathbf{u}}} \Delta \ddot{\mathbf{u}} \\ + \frac{\partial \boldsymbol{\phi}_{res}}{\partial \mathbf{f}} \Delta \mathbf{f} = \\ = \boldsymbol{\phi}_{res}(\mathbf{u}_0, \ddot{\mathbf{u}}_0, \mathbf{f}_0) + \frac{\partial \mathbf{F}_{int}}{\partial \mathbf{u}} \Delta \mathbf{u} \\ + \frac{\partial}{\partial \ddot{\mathbf{u}}} (\mathbf{M}\ddot{\mathbf{u}}) \Delta \ddot{\mathbf{u}} - \frac{\partial \mathbf{F}_{ext}}{\partial \mathbf{f}} \Delta \mathbf{f} = \\ = \boldsymbol{\phi}_{res}(\mathbf{u}_0, \ddot{\mathbf{u}}_0, \mathbf{f}_0) + \mathbf{K}_T \Delta \mathbf{u} + \mathbf{M} \Delta \ddot{\mathbf{u}} \\ - \Delta \lambda \mathbf{f}^{rif} \quad (37)$$

In Eq. (37), the finite variation of the internal forces vector is expressed by the definition of *tangent stiffness matrix*, the hypothesis of the constant mass matrix is exploited in the definition of the linearized contribution of inertia load, and the hypothesis of conservative loads is considered writing then the finite variation of external forces vector as the variation of the *load factor*. The three terms in this final equation are related to the finite variation of internal, external, and inertial work, respectively. The linearization of the internal work is carried out considering a generic finite increment of the nodal displacement vector and a first-order truncated Taylor expansion of the internal forces contribution. The FN of the tangent stiffness matrix, under CUF formalism, can be defined as follows:

$$\Delta(\delta \mathcal{L}_{int}) = \Delta \left( \int_{\Omega} \delta \mathbf{E}^T \mathbf{S} dV \right) = \int_{\Omega} \delta \mathbf{E}^T \Delta \mathbf{S} dV + \int_{\Omega} \Delta(\delta \mathbf{E}^T) \mathbf{S} dV = \\ = \delta \mathbf{u}_{sj}^T \mathbf{K}_{ll}^{\tau sij} \Delta \mathbf{u}_{\tau i} + \delta \mathbf{u}_{sj}^T \mathbf{K}_{T1}^{\tau sij} \Delta \mathbf{u}_{\tau i} + \delta \mathbf{u}_{sj}^T \mathbf{K}_{\sigma}^{\tau sij} \Delta \mathbf{u}_{\tau i} \\ = \delta \mathbf{u}_{sj}^T \mathbf{K}_T^{\tau sij} \Delta \mathbf{u}_{\tau i} \quad (38)$$

where  $\mathbf{K}_{ll}^{\tau sij}$  is the FN of the linear stiffness matrix,  $\mathbf{K}_{T1}^{\tau sij}$  is the FN of the nonlinear contribution of the tangent stiffness matrix, and  $\mathbf{K}_{\sigma}^{\tau sij}$  is the FN of the geometrical stiffness matrix. Considering the summation over the indices and CUF assembling procedure as previously addressed, the second term of Eq. (37) is obtained. The complete derivation of the analytic expression of the tangent stiffness matrix FN for hyperelastic

material can be found in [20,22]. The linearized form of the inertial contribution of the variational principle is exploited again through the hypothesis of the constant mass matrix considering the same derivation procedure, by a Taylor expansion truncated at the first order around a known equilibrium condition:

$$\begin{aligned}\Delta(\delta\mathcal{L}_{ine}) &= \Delta(\delta\mathbf{u}_{sj}^T \mathbf{M}^{\tau sij} \ddot{\mathbf{u}}_{\tau i}) = \delta\mathbf{u}_{sj}^T \Delta\mathbf{M}^{\tau sij} \ddot{\mathbf{u}}_{\tau i} + \delta\mathbf{u}_{sj}^T \mathbf{M}^{\tau sij} \Delta\ddot{\mathbf{u}}_{\tau i} \\ &= \delta\mathbf{u}_{sj}^T \mathbf{M}^{\tau sij} \Delta\ddot{\mathbf{u}}_{\tau i}\end{aligned}\quad (39)$$

Given the definitions of linearized energetic contributions, at each generic non-trivial equilibrium state, the condition  $\phi_{res}(\mathbf{u} + \Delta\mathbf{u}, \ddot{\mathbf{u}}_0 + \Delta\ddot{\mathbf{u}}, \mathbf{f}_0 + \Delta\mathbf{f}) = 0$  is fulfilled. The nonlinear governing equation for the displacements, accelerations, and nodal forces increments is rewritten as follows:

$$\mathbf{K}_T \Delta\mathbf{u} + \mathbf{M} \Delta\ddot{\mathbf{u}} = -\phi_{res}(\mathbf{u}_0, \ddot{\mathbf{u}}_0, \mathbf{f}_0) + \mathbf{I} \Delta\lambda \mathbf{f}^{rif} \quad (40)$$

For a quasi-static nonlinear analysis, for which the inertial contribution is negligible, coupling Eq. (40) with a displacement–load increment constraint since  $\Delta\lambda$  is an additional variable of the problem, the numerical iterative scheme is represented by this last system of equations

$$\begin{cases} \mathbf{K}_T \Delta\mathbf{u} = -\phi_{res}(\mathbf{u}_0, \ddot{\mathbf{u}}_0, \mathbf{f}_0) + \Delta\lambda \mathbf{f}^{rif} \\ c(\Delta\mathbf{u}, \Delta\mathbf{f}) = 0 \end{cases} \quad (41)$$

This last equation is solved iteratively, updating the unbalanced nodal forces vector considering the provisional iteration step solution, until the nodal displacement and forces increments satisfy condition  $\phi_{res}(\mathbf{u}, \ddot{\mathbf{u}}, \mathbf{f}) = 0$ , up to a certain convergence tolerance. The constraint equation characterizes the numerical scheme adopted, one can implement displacement control, load control, and path-following methods by adopting a different constraint. In the present work, the path-following method proposed by Crisfield [35] is employed, and the implementation of such arc-length iterative solver in a CUF-based finite element scenario is described in detail in [28]. In the context of arc-length-based numerical solvers for nonlinear algebraic systems of equations, the additional equation governing the nodal displacement increment within the path-following approach corresponds to a multi-dimensional constraint represented by the equation of a sphere. This sphere is centered at  $\mathbf{u}_0$  with a radius equal to  $L_0$ , defined as follows:

$$(L_0)^2 = (\Delta\mathbf{u}^{(k)}) \cdot (\Delta\mathbf{u}^{(k)}) \quad (42)$$

Here, the subscript  $(k)$  denotes the generic  $k$ th internal iteration on the considered load step. The above expression establishes a constraint relation for the potential generic increment of the non-trivial solution, simultaneously restricting the possible increment  $\Delta\lambda$ . Eq. (42) serves as the foundational equation for deriving the corresponding constraint equation for the load factor increment. For a more comprehensive examination of path-following methods and arc-length type solvers, the reader can refer to [36].

For an undamped vibration analysis instead, since the structure is already considered at equilibrium, all the unbalanced nodal vectors contributions of Eq. (37) are null, and no load variations are considered on the structure thus also  $\Delta\lambda = 0$ . Under these conditions, the governing equation for the free-vibration problem is:

$$\mathbf{K}_T \Delta\mathbf{u} + \mathbf{M} \Delta\ddot{\mathbf{u}} = 0 \quad (43)$$

Imposing a generic harmonic behavior of the nodal displacement increment of the form  $\Delta\mathbf{u} = \Phi e^{i\omega t}$ , the well-known linear eigenvalue problem of linearized vibrations is obtained:

$$\mathbf{K}_T \Phi e^{i\omega t} - \omega^2 \mathbf{M} \Phi e^{i\omega t} = 0 \quad (44)$$

$$(\mathbf{K}_T - \omega^2 \mathbf{M}) \Phi e^{i\omega t} = 0 \quad (45)$$

$$(\mathbf{K}_T - \omega^2 \mathbf{M}) \Phi = 0 \quad (46)$$

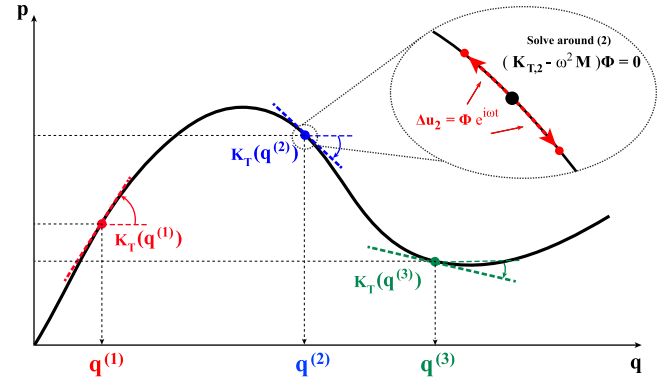


Fig. 3. Linearized vibration problem around equilibrium state: graphical interpretation.

Eq. (46) corresponds to the classical eigenvalue problem in the small-amplitude free vibration problem around the trivial equilibrium state, solved numerically employing already available libraries and packages based on the Arnoldi algorithm for eigenvalue computation. After the computation of the tangent stiffness matrix in the chosen non-trivial equilibrium state, the linear eigenvalues problem is then uniquely defined and thereafter solved, obtaining the natural frequencies and modal shapes of vibration around the equilibrium state (different from the trivial one) since the eigenvalues (or modal shapes) coming from the solution of Eq. (46) are the harmonic increments of displacement variables from the deformed state. Fig. 3 shows the geometrical representation of the algorithm presented in this work.

## 5. Numerical results

The accuracy of proposed higher-order 1D CUF-based finite elements for hyperelasticity is now established in this section, analyzing different case studies of undamped vibration problems in trivial and non-trivial equilibrium states of beam structures. In this work, the modal behavior of isotropic compressible and nearly-incompressible soft materials is investigated, and the actual results are compared with consistent solutions computed using commercial software. The effect of large strains on the undamped natural frequencies of hyperelastic structures is investigated, and also the influence of the mathematical model adopted in the finite element discretization on mode detection is discussed.

### 5.1. Free-vibration of a neo-Hookean thick and thin beam

The first study case is the free vibration analysis of a rectangular cross-section compressible beam. Small amplitude vibrations around the undeformed configuration are now investigated for different geometrical configurations and material conditions. Natural frequencies of the double-clamped square cross-section beam of height  $h = 10$  mm and thickness  $t = 6$  mm are investigated in two different geometrical conditions: a thick beam for which the slender ratio  $L/h = 10$  and a thin beam for which instead  $L/h = 100$ . Geometry and boundary conditions are depicted in Fig. 4.

Material is modeled with the decoupled Neo-Hookean isochoric strain energy function and the classical quadratic model for the volumetric component:

$$\Psi = \Psi_{vol}(J) + \bar{\Psi}(\bar{I}_1) = \frac{k}{2}(J - 1)^2 + \frac{\mu}{2}(\bar{I}_1 - 3) \quad (47)$$

where  $\mu$  is the infinitesimal shear modulus, for all the simulation set equal to 50 MPa,  $k$  is the bulk modulus, set to  $k = 2/3\mu$ , in a resulting Poisson's ratio  $\nu = (3k - 2\mu)/(2(3k + 2\mu)) = 0$ . In all further investigations of this case study, the material density of the hyperelastic beam is set to a typical value of silicone rubber, thus  $\rho = 1340$  kg/m<sup>3</sup>.

**Table 1**

Compressible beam, case  $L/h = 10$ : convergence analysis on natural frequencies [Hz]. In brackets, the percentage difference between the proposed models and the 3D elasticity solution is given.

Mode	LE-2 (parabolic model)				LE-3 (cubic model)				3D ABQ
	5B4	10B4	15B4	20B4	5B4	10B4	15B4	20B4	C8D20RH
1	165.776 <sup>(0.297%)</sup>	165.748 <sup>(0.003%)</sup>	165.747 <sup>(0.280%)</sup>	165.747 <sup>(0.280%)</sup>	165.327 <sup>(0.025%)</sup>	165.290 <sup>(0.003%)</sup>	165.287 <sup>(0.001%)</sup>	165.285 <sup>(0.000%)</sup>	165.285
2	268.728 <sup>(0.731%)</sup>	268.707 <sup>(0.723%)</sup>	268.707 <sup>(0.723%)</sup>	268.707 <sup>(0.723%)</sup>	266.849 <sup>(0.026%)</sup>	266.796 <sup>(0.007%)</sup>	266.789 <sup>(0.004%)</sup>	266.785 <sup>(0.003%)</sup>	266.778
3	447.768 <sup>(0.713%)</sup>	447.199 <sup>(0.585%)</sup>	447.188 <sup>(0.583%)</sup>	447.187 <sup>(0.582%)</sup>	445.269 <sup>(0.151%)</sup>	444.642 <sup>(0.010%)</sup>	444.612 <sup>(0.003%)</sup>	444.601 <sup>(0.001%)</sup>	444.597
4	702.324 <sup>(1.457%)</sup>	701.908 <sup>(1.397%)</sup>	701.900 <sup>(1.396%)</sup>	701.900 <sup>(1.395%)</sup>	693.016 <sup>(0.112%)</sup>	692.372 <sup>(0.019%)</sup>	692.323 <sup>(0.012%)</sup>	692.287 <sup>(0.007%)</sup>	692.240
5	856.881 <sup>(7.635%)</sup>	860.799 <sup>(8.128%)</sup>	860.704 <sup>(8.116%)</sup>	852.887 <sup>(7.134%)</sup>	799.437 <sup>(0.420%)</sup>	797.447 <sup>(0.170%)</sup>	797.092 <sup>(0.125%)</sup>	797.612 <sup>(0.190%)</sup>	796.096
6	861.709 <sup>(1.974%)</sup>	852.980 <sup>(0.941%)</sup>	852.894 <sup>(0.931%)</sup>	860.686 <sup>(1.853%)</sup>	849.345 <sup>(0.511%)</sup>	845.238 <sup>(0.025%)</sup>	845.089 <sup>(0.008%)</sup>	845.043 <sup>(0.002%)</sup>	845.025
7	1294.772 <sup>(2.279%)</sup>	1291.848 <sup>(2.048%)</sup>	1291.793 <sup>(2.043%)</sup>	1291.788 <sup>(2.043%)</sup>	1270.174 <sup>(0.336%)</sup>	1266.414 <sup>(0.039%)</sup>	1266.226 <sup>(0.024%)</sup>	1266.079 <sup>(0.012%)</sup>	1265.924
8	1365.896 <sup>(1.404%)</sup>	1364.976 <sup>(1.336%)</sup>	1365.896 <sup>(1.404%)</sup>	1365.896 <sup>(1.404%)</sup>	1360.741 <sup>(1.022%)</sup>	1347.720 <sup>(0.055%)</sup>	1347.175 <sup>(0.014%)</sup>	1347.035 <sup>(0.004%)</sup>	1346.981
9	1376.907 <sup>(0.806%)</sup>	1365.896 <sup>(0.000%)</sup>	1364.589 <sup>(-0.096%)</sup>	1364.555 <sup>(-0.098%)</sup>	1365.896 <sup>(0.000%)</sup>	1365.896 <sup>(0.000%)</sup>	1365.896 <sup>(0.000%)</sup>	1365.896 <sup>(0.000%)</sup>	1365.896
10	1724.067 <sup>(8.242%)</sup>	1722.166 <sup>(8.123%)</sup>	1721.977 <sup>(8.111%)</sup>	1721.941 <sup>(8.109%)</sup>	1599.650 <sup>(0.431%)</sup>	1595.535 <sup>(0.173%)</sup>	1594.822 <sup>(0.128%)</sup>	1595.871 <sup>(0.194%)</sup>	1592.787
DOFs	432	837	1242	1647	768	1488	2208	2928	13086

**Table 2**

Compressible beam case  $L/h = 10$ : effect of the expansion theory on natural frequencies [Hz]. The percentage difference between proposed results and the 3D elasticity solution is reported in brackets.

Mode	1D CUF, Expansion theory						3D ABQ
	TE-1	TE-2	TE-3	TE-4	LE-2	LE-3	C8D20RH
1	165.747 <sup>(0.280%)</sup>	165.747 <sup>(0.280%)</sup>	165.286 <sup>(0.000%)</sup>	165.285 <sup>(0.000%)</sup>	165.747 <sup>(0.280%)</sup>	165.285 <sup>(0.000%)</sup>	165.285
2	268.707 <sup>(0.723%)</sup>	268.707 <sup>(0.723%)</sup>	266.788 <sup>(0.003%)</sup>	266.785 <sup>(0.003%)</sup>	268.707 <sup>(0.723%)</sup>	266.785 <sup>(0.003%)</sup>	266.778
3	447.187 <sup>(0.582%)</sup>	447.187 <sup>(0.582%)</sup>	444.605 <sup>(0.002%)</sup>	444.601 <sup>(0.001%)</sup>	447.187 <sup>(0.582%)</sup>	444.601 <sup>(0.001%)</sup>	444.597
4	701.900 <sup>(1.395%)</sup>	701.900 <sup>(1.395%)</sup>	692.311 <sup>(0.010%)</sup>	692.287 <sup>(0.007%)</sup>	701.900 <sup>(1.395%)</sup>	692.287 <sup>(0.007%)</sup>	692.240
5	852.887 <sup>(7.134%)</sup>	852.887 <sup>(7.134%)</sup>	860.435 <sup>(8.082%)</sup>	797.612 <sup>(0.190%)</sup>	852.887 <sup>(7.134%)</sup>	797.612 <sup>(0.190%)</sup>	796.096
6	965.834 <sup>(14.297%)</sup>	860.686 <sup>(1.853%)</sup>	845.058 <sup>(0.004%)</sup>	845.043 <sup>(0.002%)</sup>	860.686 <sup>(1.853%)</sup>	845.043 <sup>(0.002%)</sup>	845.025
7	1291.788 <sup>(2.043%)</sup>	1291.788 <sup>(2.043%)</sup>	1266.185 <sup>(0.021%)</sup>	1266.079 <sup>(0.012%)</sup>	1291.788 <sup>(2.043%)</sup>	1266.079 <sup>(0.012%)</sup>	1265.924
8	1365.896 <sup>(1.404%)</sup>	1364.555 <sup>(1.305%)</sup>	1347.083 <sup>(0.008%)</sup>	1347.035 <sup>(0.004%)</sup>	1365.896 <sup>(1.404%)</sup>	1347.035 <sup>(0.004%)</sup>	1346.981
9	1364.555 <sup>(-0.098%)</sup>	1365.896 <sup>(0.000%)</sup>	1365.896 <sup>(0.000%)</sup>	1365.896 <sup>(0.000%)</sup>	1364.555 <sup>(-0.098%)</sup>	1365.896 <sup>(0.000%)</sup>	1365.896
10	1931.669 <sup>(21.276%)</sup>	1721.941 <sup>(8.109%)</sup>	1720.951 <sup>(8.046%)</sup>	1595.871 <sup>(0.194%)</sup>	1721.941 <sup>(8.109%)</sup>	1595.871 <sup>(0.194%)</sup>	1592.787
DOFs	549	1098	1830	2745	1242	1647	13086

**Table 3**

Compressible beam, case  $L/h = 100$ : convergence analysis on natural frequencies [Hz]. In brackets, the percentage difference between the proposed models and the 3D elasticity solution is given.

Mode	LE-2 (parabolic model)				LE-3 (cubic model)				3D ABQ
	5B4	10B4	15B4	20B4	5B4	10B4	15B4	20B4	C8D20RH
1	1.685 <sup>(0.057%)</sup>	1.685 <sup>(0.000%)</sup>	1.685 <sup>(0.004%)</sup>	1.685 <sup>(0.003%)</sup>	1.685 <sup>(0.054%)</sup>	1.685 <sup>(0.003%)</sup>	1.685 <sup>(0.001%)</sup>	1.685 <sup>(0.000%)</sup>	1.685
2	2.808 <sup>(0.060%)</sup>	2.807 <sup>(0.011%)</sup>	2.807 <sup>(0.009%)</sup>	2.807 <sup>(0.008%)</sup>	2.808 <sup>(0.052%)</sup>	2.807 <sup>(0.003%)</sup>	2.807 <sup>(0.001%)</sup>	2.807 <sup>(0.000%)</sup>	2.807
3	4.661 <sup>(0.397%)</sup>	4.644 <sup>(0.031%)</sup>	4.643 <sup>(0.011%)</sup>	4.643 <sup>(0.008%)</sup>	4.660 <sup>(0.391%)</sup>	4.643 <sup>(0.024%)</sup>	4.642 <sup>(0.004%)</sup>	4.642 <sup>(0.001%)</sup>	4.642
4	7.761 <sup>(0.395%)</sup>	7.734 <sup>(0.039%)</sup>	7.732 <sup>(0.021%)</sup>	7.732 <sup>(0.019%)</sup>	7.760 <sup>(0.377%)</sup>	7.732 <sup>(0.021%)</sup>	7.731 <sup>(0.004%)</sup>	7.731 <sup>(0.001%)</sup>	7.731
5	9.222 <sup>(1.367%)</sup>	9.107 <sup>(0.102%)</sup>	9.100 <sup>(0.028%)</sup>	9.099 <sup>(0.016%)</sup>	9.220 <sup>(1.354%)</sup>	9.106 <sup>(0.091%)</sup>	9.099 <sup>(0.017%)</sup>	9.098 <sup>(0.005%)</sup>	9.097
6	15.343 <sup>(2.074%)</sup>	15.071 <sup>(0.261%)</sup>	15.041 <sup>(0.062%)</sup>	15.145 <sup>(0.758%)</sup>	15.354 <sup>(2.146%)</sup>	15.068 <sup>(0.243%)</sup>	15.038 <sup>(0.045%)</sup>	15.141 <sup>(0.727%)</sup>	15.031
7	15.356 <sup>(1.429%)</sup>	15.157 <sup>(0.111%)</sup>	15.147 <sup>(0.044%)</sup>	15.036 <sup>(0.689%)</sup>	15.338 <sup>(1.305%)</sup>	15.152 <sup>(0.080%)</sup>	15.142 <sup>(0.013%)</sup>	15.033 <sup>(0.706%)</sup>	15.140
8	25.528 <sup>(13.754%)</sup>	22.566 <sup>(0.553%)</sup>	22.469 <sup>(0.124%)</sup>	22.453 <sup>(0.052%)</sup>	25.517 <sup>(13.703%)</sup>	22.560 <sup>(0.526%)</sup>	22.464 <sup>(0.099%)</sup>	22.448 <sup>(0.028%)</sup>	22.442
9	25.703 <sup>(2.829%)</sup>	25.061 <sup>(0.262%)</sup>	25.016 <sup>(0.082%)</sup>	25.009 <sup>(0.056%)</sup>	25.687 <sup>(2.765%)</sup>	25.049 <sup>(0.213%)</sup>	25.004 <sup>(0.035%)</sup>	24.998 <sup>(0.009%)</sup>	24.996
10	38.179 <sup>(21.887%)</sup>	31.644 <sup>(1.023%)</sup>	31.394 <sup>(0.224%)</sup>	31.351 <sup>(0.087%)</sup>	38.152 <sup>(21.801%)</sup>	31.632 <sup>(0.984%)</sup>	31.383 <sup>(0.190%)</sup>	31.341 <sup>(0.055%)</sup>	31.324
DOFs	432	837	1242	1647	768	1488	2208	2928	9558

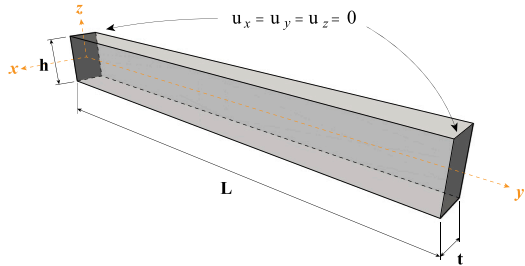


**Fig. 4.** Double clamped Neo-Hookean beam: geometrical features and boundary conditions.

As a preliminary investigation, convergence analysis is carried out considering different 1D CUF-based beam models for the thick and thin beam case. For each kinematic discretization employed for the beam axis, different cross-section expansion polynomials are considered. From now on, these definitions will be referred to bilinear,

quadratic, and cubic beam axis models as B2, B3, and B4; cross-section approximation by a single bilinear, quadratic, and cubic model will be addressed as LE-2 (four nodes), LE-3 (nine nodes) and LE-4 (sixteen nodes). The geometrical representation of some 1D CUF beam models employed in the present analysis is reported in Fig. 5. Actual numerical results obtained adopting 1D CUF elements are compared with the numerical results obtained by the ABAQUS commercial software. Reference results for the thick beam were obtained adopting 750 C3D20RH hexahedral elements (20-node quadratic brick coupled with hybrid formulation, linear pressure interpolation, and reduced integration); instead, 334 C3D20RH were employed in the computation of reference solution for the thin beam. The total degrees of freedom (DOFs) for each mathematical model adopted in 1D-CUF discretization and 3D ABAQUS models will be compared.

Tables 1 and 2 show the convergence analysis carried out in the case of a thick beam; both convergences achieved incrementing the number of the finite element along the axis and effects of the expansion theory are investigated. The same investigation is carried out in the



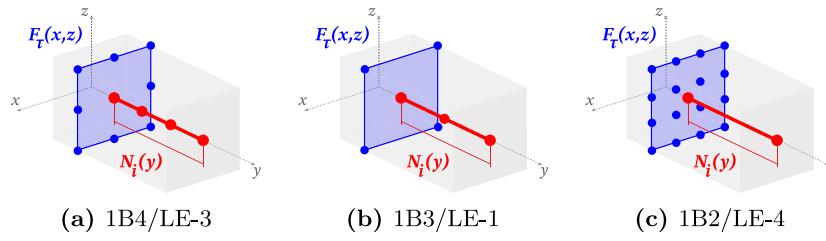


Fig. 5. Double clamped neo-Hookean beam: examples of 1D beam 1D CUF elements adopted.

Table 4

Compressible beam, case  $L/h = 100$ : effect of the expansion theory on natural frequencies [Hz]. The percentage difference between proposed results and the 3D elasticity solution is reported in brackets.

Mode	1D CUF, Expansion theory						3D ABQ
	TE-1	TE-2	TE-3	TE-4	LE-2	LE-3	C8D20RH
1	1.685 <sup>(0.003%)</sup>	1.685 <sup>(0.003%)</sup>	1.685 <sup>(0.000%)</sup>	1.685 <sup>(0.000%)</sup>	1.685 <sup>(0.000%)</sup>	1.685 <sup>(0.000%)</sup>	1.685
2	2.807 <sup>(0.008%)</sup>	2.807 <sup>(0.008%)</sup>	2.807 <sup>(0.000%)</sup>	2.807 <sup>(0.000%)</sup>	2.807 <sup>(0.000%)</sup>	2.807 <sup>(0.000%)</sup>	2.807
3	4.643 <sup>(0.008%)</sup>	4.643 <sup>(0.008%)</sup>	4.642 <sup>(0.001%)</sup>	4.642 <sup>(0.001%)</sup>	4.643 <sup>(0.008%)</sup>	4.642 <sup>(0.001%)</sup>	4.642
4	7.732 <sup>(0.019%)</sup>	7.732 <sup>(0.019%)</sup>	7.731 <sup>(0.001%)</sup>	7.731 <sup>(0.001%)</sup>	7.732 <sup>(0.019%)</sup>	7.731 <sup>(0.001%)</sup>	7.731
5	9.099 <sup>(0.016%)</sup>	9.099 <sup>(0.016%)</sup>	9.098 <sup>(0.005%)</sup>	9.098 <sup>(0.005%)</sup>	9.099 <sup>(0.016%)</sup>	9.098 <sup>(0.005%)</sup>	9.097
6	15.036 <sup>(0.030%)</sup>	15.036 <sup>(0.030%)</sup>	15.141 <sup>(0.727%)</sup>	15.033 <sup>(0.013%)</sup>	15.145 <sup>(0.758%)</sup>	15.141 <sup>(0.727%)</sup>	15.031
7	15.145 <sup>(0.034%)</sup>	15.145 <sup>(0.034%)</sup>	15.033 <sup>(-0.706%)</sup>	15.141 <sup>(0.004%)</sup>	15.036 <sup>(-0.689%)</sup>	15.033 <sup>(-0.706%)</sup>	15.140
8	22.453 <sup>(0.052%)</sup>	22.453 <sup>(0.052%)</sup>	22.448 <sup>(0.028%)</sup>	22.448 <sup>(0.028%)</sup>	22.453 <sup>(0.052%)</sup>	22.448 <sup>(0.028%)</sup>	22.442
9	25.009 <sup>(0.056%)</sup>	25.009 <sup>(0.056%)</sup>	24.998 <sup>(0.009%)</sup>	24.998 <sup>(0.009%)</sup>	25.009 <sup>(0.056%)</sup>	24.998 <sup>(0.009%)</sup>	24.996
10	31.351 <sup>(0.087%)</sup>	31.351 <sup>(0.087%)</sup>	31.341 <sup>(0.055%)</sup>	31.341 <sup>(0.055%)</sup>	31.351 <sup>(0.087%)</sup>	31.341 <sup>(0.055%)</sup>	31.324
DOFs	549	1098	1830	2745	1242	1647	9558

Table 5

Compressible beam, case  $L/h = 100$  and  $L/h = 10$ : comparison between natural frequencies obtained adopting the linear elastic constitutive law and hyperelastic constitutive law, frequencies in [Hz].

Mode	$L/h = 100$			$L/h = 10$		
	1D CUF	3D ABQ	1D CUF	1D CUF	3D ABQ	1D CUF
	Linear elastic	Linear elastic	Hyperelastic	Linear elastic	Linear elastic	Hyperelastic
1	1.685	1.685	1.685	165.285	165.285	165.285
2	2.807	2.807	2.807	266.785	266.778	266.785
3	4.642	4.642	4.642	444.601	444.597	444.601
4	7.731	7.731	7.731	692.287	692.240	692.287
5	9.098	9.097	9.098	797.612	796.096	797.612
6	15.141	15.031	15.141	845.043	845.025	845.043
7	15.033	15.140	15.033	1266.078	1265.924	1266.079
8	22.448	22.442	22.448	1347.035	1346.981	1347.035
9	24.998	24.996	24.998	1365.896	1365.896	1365.896
10	31.341	31.324	31.341	1595.871	1592.787	1595.871

case of the thin beam with a slender ratio  $L/h = 100$ , and results are listed in Tables 3 and 4. For coarser discretizations, adopting a few finite elements along the beam axis, evident discrepancies concerning reference results are observed, and not all the investigated models are able to capture the global frequency behavior of the beam in both geometrical configurations considered. Therefore, from now on, 20 B4 elements along the axis of the beam will be employed in further analysis. Clearly, for very elongated structures, all Taylor models can capture correctly all the frequencies while also adopting lower order models, results are in perfect agreement with the reference one. Still, this result is not achieved anymore in the case of the thick beam, for which higher order models (TE-3, TE-4, and LE-3) are necessary to compute accurate results. Thus, from now on, only LE-4 cubic expansion models will be adopted for further analysis.

For verification purposes, since the undamped vibration problem is analyzed around the trivial equilibrium state, these last analysis are compared with the classical linear eigenvalue problem for a linearly elastic material around the undeformed state. Adopting the same 1D CUF model made of 20B4-LE-3 and 3D ABAQUS models described before, the natural frequencies of the equivalent linear elastic materials with Poisson's ratio  $\nu = 0$  and Young's modulus  $E = 2\mu(1 + \nu) = 2\mu$  are investigated in both  $L/h = 100$  and  $L/h = 10$  configurations. Table 5 compares the natural frequencies of the linear elastic beams with the

previously obtained results starting from a hyperelastic constitutive law. A perfect match is observed.

## 5.2. Cantilever beam subjected to bending and shear

The second case study is the modal analysis of a cantilever square cross-section beam in non-trivial equilibrium conditions. The beam is subjected to two vertical concentrated loads at the tip free-end. The modal analysis is performed around different deformed configurations for increasing values of external load. The equilibrium path is computed first by performing a static nonlinear analysis, considering the beam in different material compressibility conditions. Furthermore, in each non-trivial equilibrium state, the influence of the compressibility on natural frequencies and modal shapes is investigated with a modal analysis in the chosen interested point. Geometrical features, boundary conditions, and discretization model adopted are shown in Fig. 6.

Material is modeled again with the same Neo-Hookean strain energy density function Eq. (47) already defined in the previous case. Material parameters  $k$  and  $\mu$  are chosen in such a way the resulting Poisson's ratio tends to the limit value of  $\nu = 0.5$ , starting from a compressible material condition with  $\nu = 0.125$ . Material constants considered in each case are reported in Table 6. The material density of the hyperelastic beam is the same as the previous case study, thus again set to

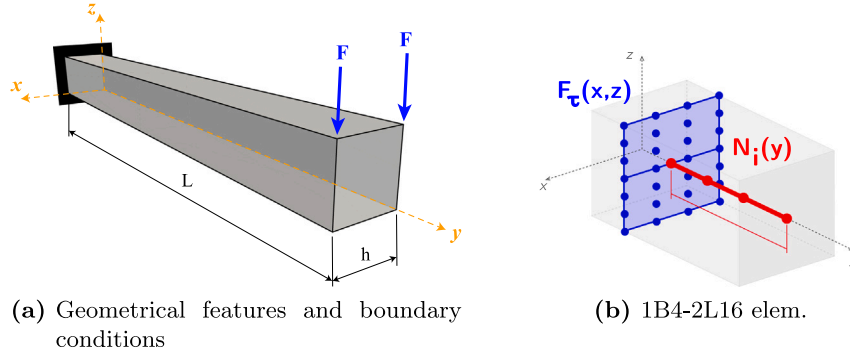


Fig. 6. Cantilever Neo-Hookean beam: geometry, boundary conditions and discretization.

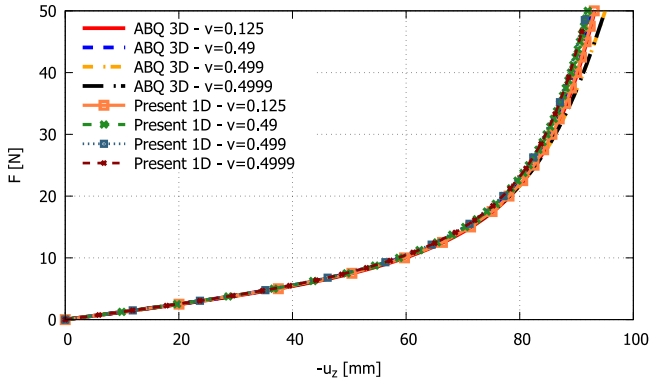


Fig. 7. Cantilever square cross-section beam: equilibrium paths for all material conditions.

Table 6

Cantilever Neo-Hookean beam: material properties for different compressibility conditions.

	E [MPa]	$D_1 = 2/k$ [MPa <sup>-1</sup> ]	$\nu$	$\mu$ [MPa]
Compressible	100	$4.5 \cdot 10^{-2}$	0.125	44.444
Nearly-incompressible, case 1	100	$1.2 \cdot 10^{-3}$	0.49	33.557
Nearly-incompressible, case 2	100	$1.2 \cdot 10^{-4}$	0.499	33.355
Nearly-incompressible, case 3	100	$1.2 \cdot 10^{-5}$	0.4999	33.355

$\rho = 1340 \text{ kg/m}^3$ . Reference results are obtained by ABAQUS commercial finite element code, adopting the same discretization adopted for the previous study case described in Section 5.1, instead actual results obtained by the presented implementation of high order CUF models are obtained considering now 20B4 - 2LE-3 1D CUF elements for convergence reason and volumetric locking prevention. Fig. 7 illustrates the equilibrium path of the cantilever beam for each material condition, analyzing the modulus of vertical tip displacement versus the modulus of the single load value applied, and comparing the nonlinear path of each case considered.

In particular, different values of vertical displacement of the tip-free end for different load values applied are listed in Table 7, where the actual 1D CUF equilibrium path is compared to the 3D ABAQUS solution. Minor differences are observed at extremely deformed configurations due to local effects. Furthermore, the modal analysis in the same non-trivial state is conducted for all different compressibility conditions considered. In the first investigations, dependence on load conditions and deformed configuration is analyzed. The undamped vibration problem is solved around different non-trivial equilibrium states, obtaining the associated natural frequencies for each material condition under analysis.

Table 8 lists the first five modes in each material condition in two different deformed configurations. Significant differences are observed

Table 7

Cantilever square cross-section beam: vertical tip displacement for different load values and material conditions [mm]. Comparison between 3D ABAQUS model results and 1D CUF results.

	F = 5 N		F = 10 N		F = 20 N	
	1D CUF	3D ABQ	1D CUF	3D ABQ	1D CUF	3D ABQ
$\nu = 0.125$	-37.5140	-37.8263	-59.7240	-60.2539	-78.1179	-78.9955
$\nu = 0.49$	-36.6995	-37.3115	-58.7537	-59.6533	-77.1931	-78.4105
$\nu = 0.499$	-36.6035	-37.1045	-58.6403	-59.4295	-77.1168	-78.2279
$\nu = 0.4999$	-36.6480	-37.0770	-58.8465	-59.3996	-77.1154	-78.2030

Table 8

Cantilever square cross-section beam: natural frequencies in non-trivial equilibrium states for different material conditions [Hz].

	F = 10 N				
	Mode 1	Mode 2	Mode 3	Mode 4	Mode 5
$\nu = 0.125$	51.983	55.394	248.576	272.316	403.699
$\nu = 0.49$	52.886	56.114	250.416	273.799	348.649
$\nu = 0.499$	53.459	56.876	250.209	274.392	345.918
$\nu = 0.4999$	52.787	55.998	250.693	273.831	344.717
	F = 30 N				
	Mode 1	Mode 2	Mode 3	Mode 4	Mode 5
$\nu = 0.125$	71.724	79.072	253.693	292.286	416.499
$\nu = 0.49$	72.943	79.975	254.757	287.430	367.265
$\nu = 0.499$	74.124	81.209	256.079	289.079	369.714
$\nu = 0.4999$	73.107	80.108	255.150	287.964	367.316

at higher frequency modes; the material conditions do not affect lower frequency modes. Fig. 8 shows the load-frequency plots of the first twelve natural frequencies. At low frequencies, even for highly deformed configurations, compressibility does not provide any significant effects; natural frequencies vary following almost the same behavior. Higher modes show variations with respect to the compressible cases in terms of natural frequency value, but in the nearly-incompressible regime, they show a similar global behavior. In some cases, natural frequencies are unaffected by the material compressibility conditions.

Furthermore, the free vibration problem is solved in the three different deformed configurations, specifically for load values of  $F = 5 \text{ N}$ ,  $F = 15 \text{ N}$ , and  $F = 25 \text{ N}$  for the case  $\nu = 0.125$  and  $\nu = 0.49$ . Given then the natural frequencies and the complete modal behavior of the structures in non-trivial equilibrium states, further investigations are provided in terms of Modal Assurance Criterion (MAC) by comparing the sets of eigenvectors and investigating the consistency and correlation between mode shapes to evidence differences between normal modes of vibrations of structures in different equilibrium states or material conditions. In general, given two sets  $A$  and  $B$  of eigenvectors, the MAC matrix comparing these two sets is defined as follows

$$MAC_{ij} = \frac{|\{\Phi_{A_i}\}^T \{\Phi_{B_j}\}|^2}{\{\Phi_{A_i}\}^T \{\Phi_{A_i}\} \{\Phi_{B_j}\}^T \{\Phi_{B_j}\}} \quad (48)$$

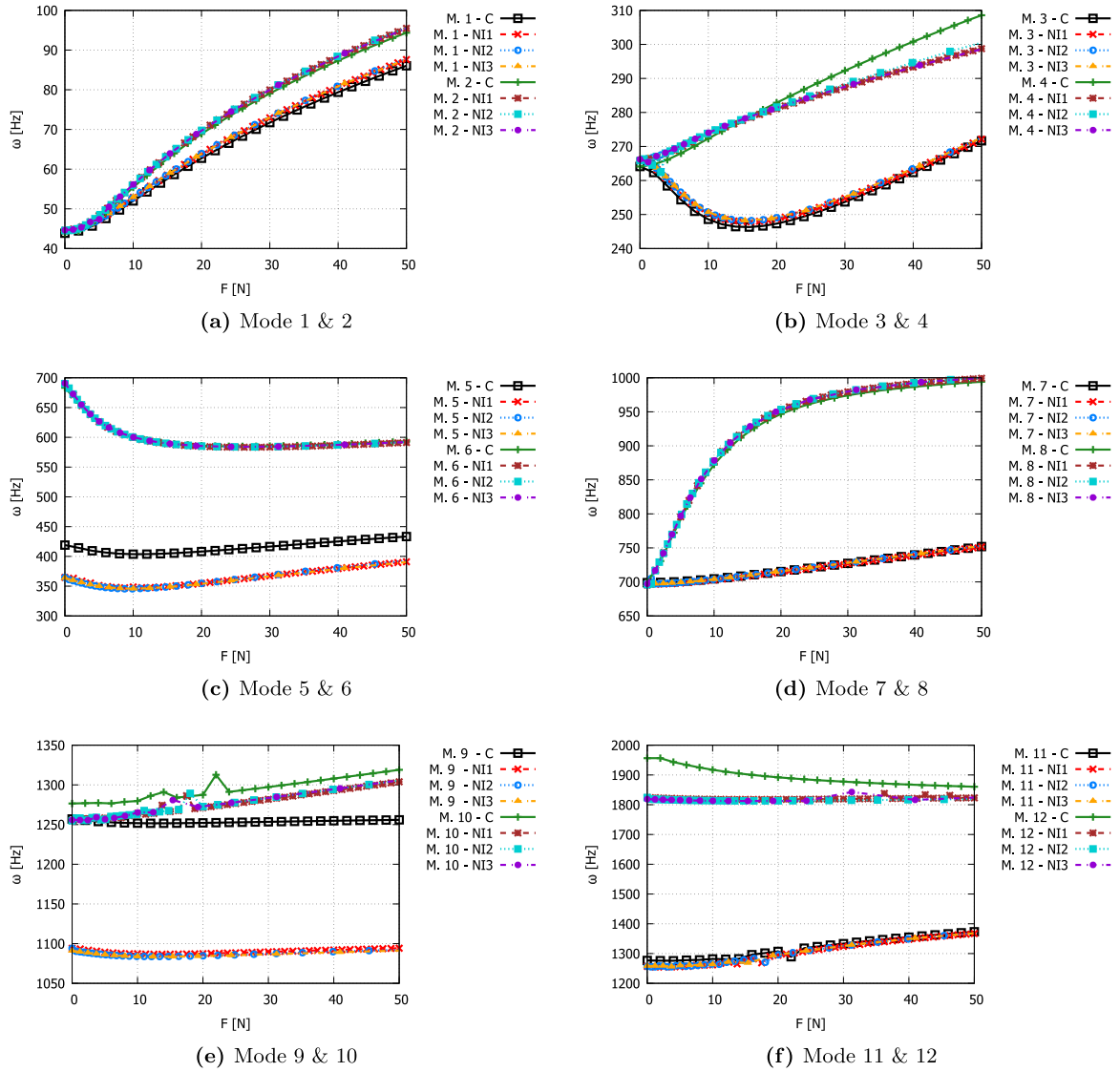


Fig. 8. Cantilever beam in non-linear equilibrium states: natural frequencies for increasing value of the free-end vertical load.

Fig. 9 shows the MAC matrix, in the case of  $\nu = 0.49$ , between mode shapes in different non-trivial equilibrium states and the undeformed configuration. The same correlation analysis is performed for the compressible material condition, and resulting MAC matrices are shown in Fig. 10. Along the equilibrium path, mode shapes are already interacting at low load values, and no additional local effects are evidenced for extremely deformed configurations. Finally, in different non-trivial equilibrium states, the correlation between modal shapes of the compressible and nearly-incompressible case of  $\nu = 0.49$  is investigated, and resulting MAC matrices are shown in Fig. 11.

### 5.3. Square cross-section beam laying on a plane

The third study case is the modal analysis of a beam laying on a horizontal plane in correspondence of its bottom surface. Small amplitude vibrations are investigated in the case of a thick beam with a side  $h = 10$  mm and slender ratio  $L/h = 10$ . Geometry, boundary conditions, and discretization model adopted are shown in Fig. 12. First, performing a free vibration analysis around the undeformed configuration, the influence of compressibility condition on the modal shapes and frequencies is investigated, then the modal behavior is analyzed when the beam is loaded with a uniform axial pressure,

Table 9

Laying Neo-Hookean beam: material properties for different compressibility conditions.

	k [MPa]	$\mu$ [MPa]	E [MPa]	$\nu$
Compressible	2.222222222	2.222222222	5	0.125
Nearly-incompressible	8333333.333	1.666666778	5	0.4999999

analyzing how natural frequencies are influenced by the non-linear equilibrium conditions.

Material is modeled again with the Neo-Hookean strain energy function Eq. (47). The beam is considered again in both compressible and nearly-incompressible material conditions by fixing the Young's modulus of the structures and varying the Poisson's ratio, the resulting material properties adopted in this case study are listed in Table 9. The material density of the hyperelastic beam is now set to  $\rho = 1150 \text{ kg/m}^3$ .

Reference results are obtained by ABAQUS commercial finite element code, with the same discretization adopted for the previous study case described in Section 5.2. Due to geometrical boundary conditions, three rigid motions are possible (translation along  $x$  and  $y$  axis, rotation about  $z$  axis). Thus the first three natural frequencies are null. Fig. 13(a) shows the value of the first 30 natural frequencies of the compressible and nearly-incompressible beam, comparing the

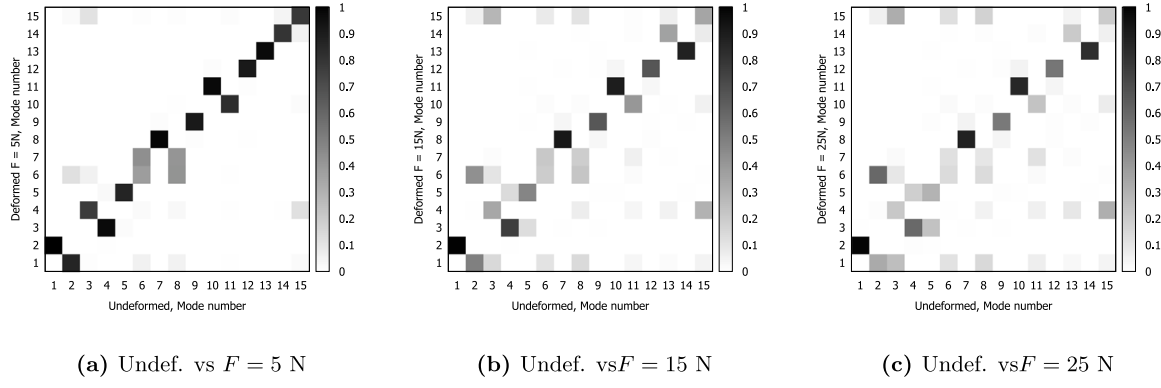


Fig. 9. Cantilever beam in non-linear equilibrium states: MAC matrix for the nearly-incompressible beam.

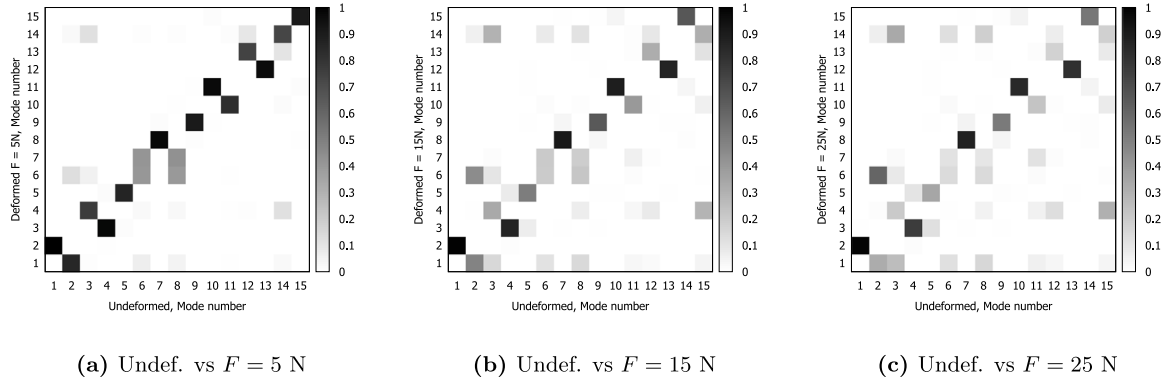


Fig. 10. Cantilever beam in non-linear equilibrium states: MAC analysis for the compressible beam.

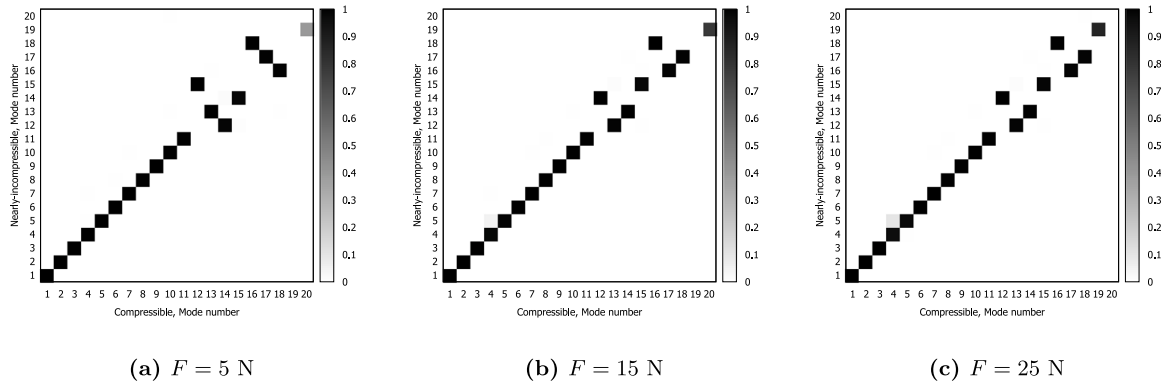


Fig. 11. Cantilever beam in non-linear equilibrium states: MAC between compressible and nearly-incompressible modal behavior in a specific nontrivial equilibrium state considered.

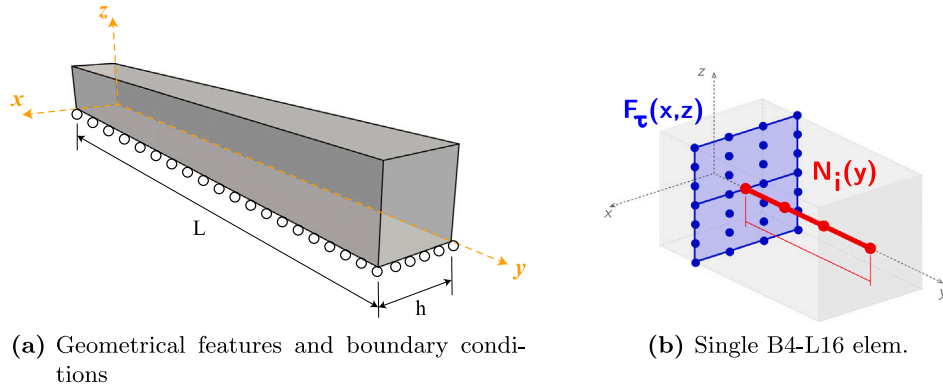


Fig. 12. Laying Neo-Hookean beam: geometry, boundary conditions and discretization.

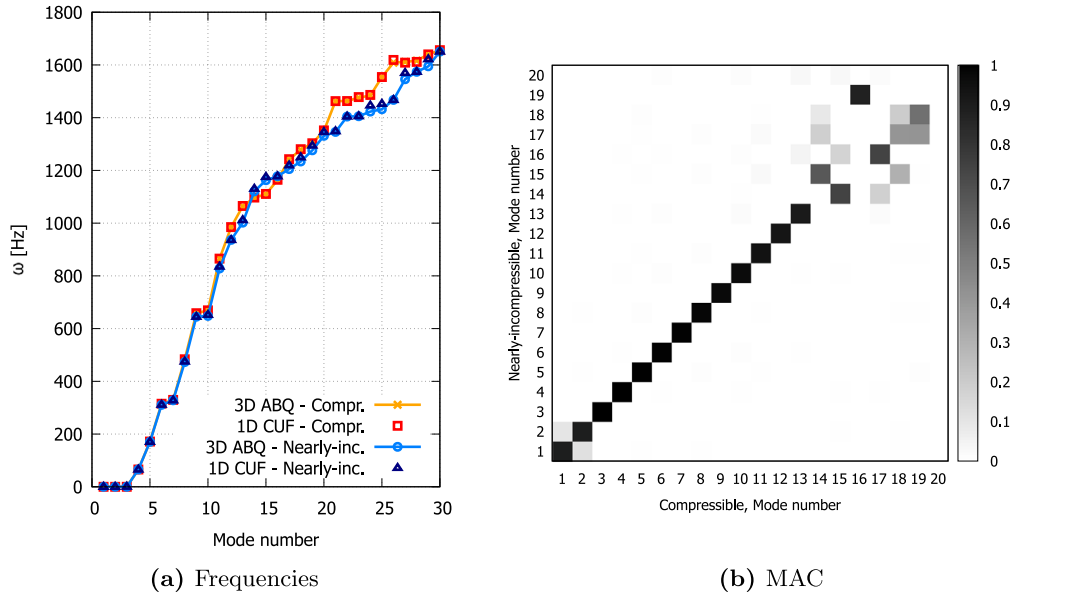


Fig. 13. Laying Neo-Hookean beam: natural frequencies in the compressible and nearly-incompressible material regime and MAC matrix comparing the two sets of solutions.

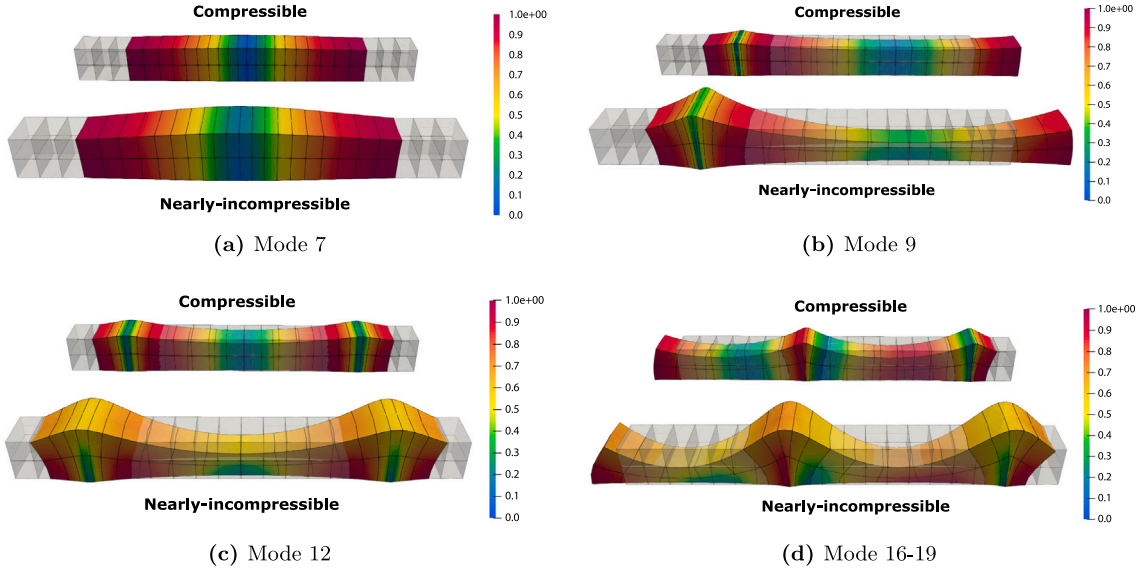


Fig. 14. Laying Neo-Hookean beam: comparison between volumetric modes in different material regimes.

actual numerical results with ABAQUS reference solution. The results are in perfect agreement; minor differences are observed in the high-frequency band. This last consideration is confirmed by the MAC matrix shown in Fig. 13(b), in which mode shapes of the compressible beam are compared with one of the nearly-incompressible beams. Interactions and energy transfer between modes are observed starting from the 13th mode, so over 1000 Hz. Special considerations are addressed about the volumetric modes of vibrations depicted in Fig. 14, which are associated with an axially moving wave along the beam axis. In the nearly-incompressible material regime, differently to the case of compressible material, the deformation gradient satisfies the incompressibility condition given by  $J = \det \mathbf{F} = 1$ ; therefore, the components of the deformation gradient are dependent from each other. Due to incompressibility, the cross-section of the peak of amplitude must shrink and dilates periodically, differently concerning the compressible case in which the components of the deformation gradient (then the displacement derivatives and so the strain tensor) are free and independent from each other.

As further analysis, the nearly-incompressible beam is analyzed, investigating the influence of prestressed equilibrium states on the modal behavior of the structure. In this particular examination, a uniform traction pressure is applied at the free end of the beam. The geometrical features, displacement boundary conditions, and load applied are depicted in Fig. 15(a). The beam discretization employed in the current analysis follows the mathematical model employed in the previous free vibration analysis. Therefore the 20 B4 - 2 LE-3 discretization is adopted. First, a nonlinear static analysis is conducted to describe the equilibrium path of the beam and the non-trivial equilibrium states around which the undamped vibration problem is then solved. Fig. 15(b) shows the equilibrium path of the beam, plotting the axial stretch  $\lambda_y$  versus the modulus of tip axial pressure applied and the distribution of  $S_{yy}$  stress component along the equilibrium path. From an analytic point of view, it can be shown that the axial component of PK2 stress tensor is a monotone increasing function that tends to the value of infinitesimal shear modulus  $\mu$  when  $\lambda_y$  tends to infinity, and this behavior is also obtained numerically.



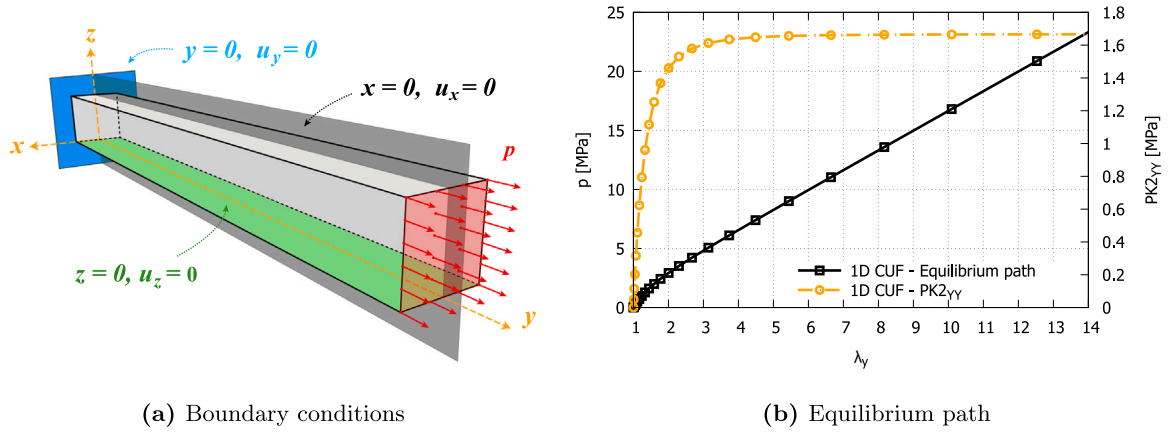


Fig. 15. Axially loaded Neo-Hookean beam: load conditions and equilibrium paths.

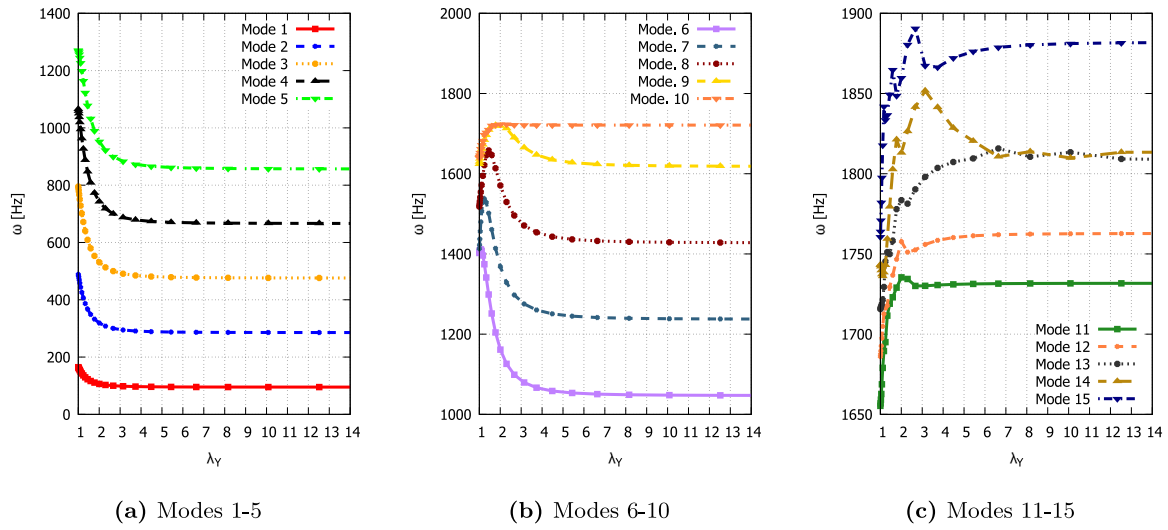


Fig. 16. Axially loaded Neo-Hookean beam: natural frequencies versus traction pressure applied.

In each representative non-trivial configuration marked in the equilibrium path, the free vibration problem is solved, investigating the influence of the principal stretch  $\lambda_y$  on the natural frequencies and mode shapes of the beam. Fig. 16 shows the stretch–frequency curve depicting the first fifteen modes function of the principal stretch ratio, instead Fig. 17 shows the same comparison in the small/moderate strain regime. Fig. 18 shows the first six normal modes of vibration for a pre-stretched condition considering  $\lambda_y = 2$ . A monotone-decreasing behavior is generally observed for the lower frequency modes. Instead, higher modes increase due to growth in axial internal stresses (influencing the resulting structure stiffness) and then decreasing monotone behavior in the high strains regime since the internal stresses are asymptotically tending to a constant value. In conclusion, due to the nonlinear constitutive behavior of the material, natural frequencies are expected to decrease since, during the load cycle, an asymptotic behavior of the internal stress  $S_{yy}$  is observed, resulting in a decreasing beam stiffness.

#### 5.4. Thin-walled box beam

The last study case is the modal analysis of a thin-walled box beam. Natural frequencies and normal modes of vibrations are investigated in the case of a beam of total length  $L = 50$  mm, cross section sides  $a = 4$  mm and  $b = 3$  mm, with an internal thickness of  $t = 0.2$  mm and clamped at both free ends. Geometry, boundary conditions, and mathematical models adopted in the discretization of the structure are

Table 10

Thin-walled box beam: material properties.

	k [MPa]	$\mu$ [MPa]	E [MPa]	$\nu$
Compressible	0.416666	0.19230	0.5	0.3
Nearly-incompressible	16.66666	0.16722	0.5	0.495

depicted in Fig. 19. The dependence on the compressibility condition of the modal behavior of the structures is investigated again, considering a compressible and nearly-incompressible material regime with the same Young's modulus. Material properties of both conditions are reported in Table 10.

Material is modeled adopting the classical Neo-Hookean strain energy function and the quadratic model for the volumetric component Eq. (47). The modal behavior of the present thin-walled beam is investigated in two different compressibility regimes, completely defined in the case of a Neo-Hookean material by the ratio between bulk modulus and infinitesimal shear modulus. By fixing the Young modulus  $E$  of the material and considering two different Poisson's ratios, the involved material constants can be found by the classical elastic relations between engineering constants. For all the simulations  $E = 50$  MPa, the remaining constants are reported in Table 10 and the material density of the hyperelastic beam is set to  $\rho = 1150$  kg/m<sup>3</sup>.

The numerical results obtained employing 1D CUF beam models are compared with ABAQUS commercial finite element code adopting solid hexahedral models. The mathematical model considered in

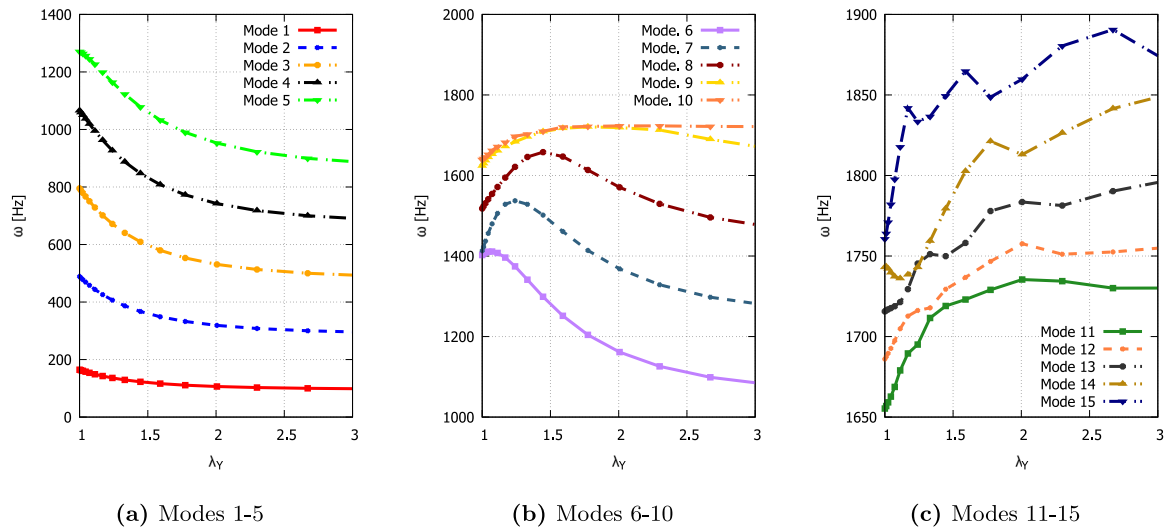


Fig. 17. Axially loaded Neo-Hookean beam: natural frequencies versus traction pressure applied, nearly-incompressible case, small/moderate stretch regime.

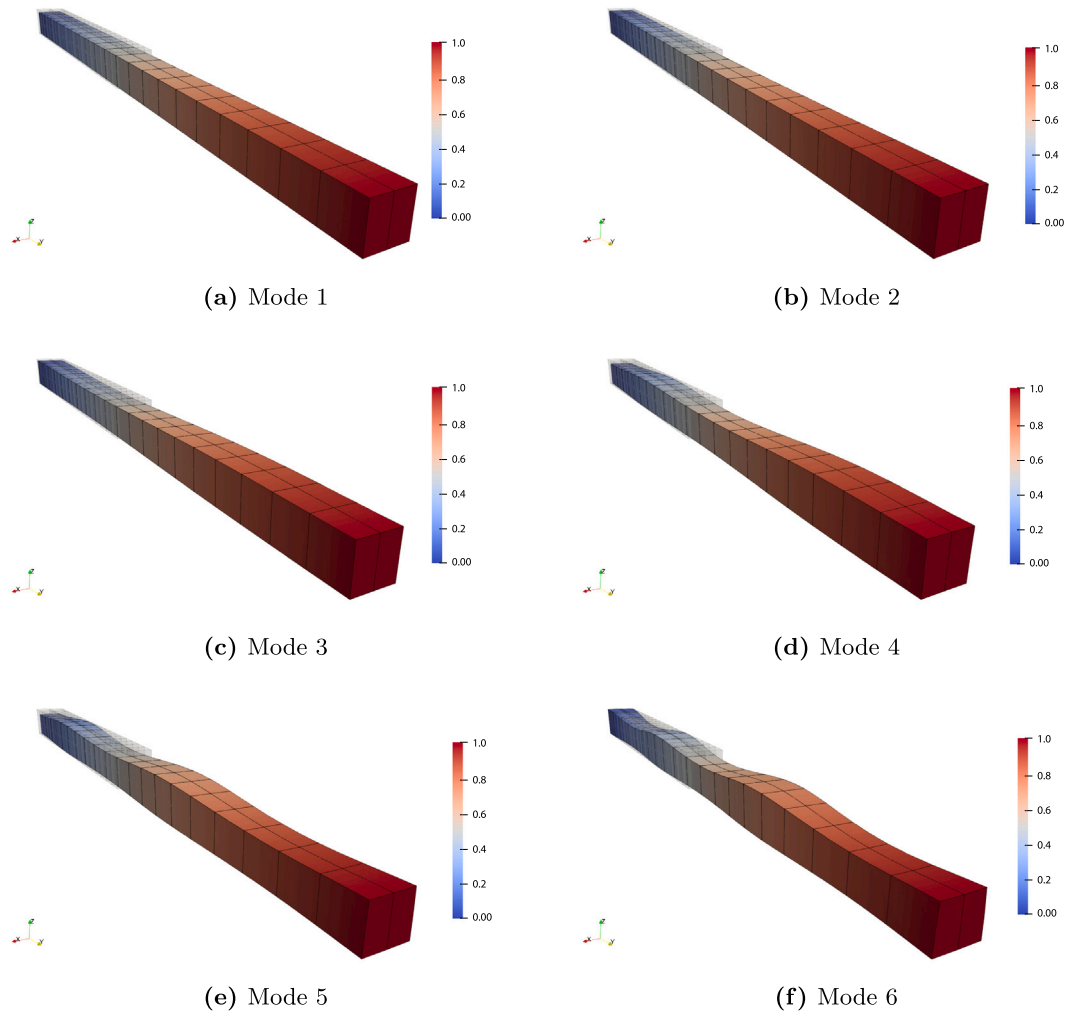


Fig. 18. Axially loaded Neo-Hookean beam: normal modes of vibrations for  $\lambda_\gamma = 2$ .

the case of 1D-CUF is made by a total number of 36 cross-section expansion elements, accounting for one element for each corner and eight elements in each straight side of the cross-section as shown in

Fig. 19(b), and considering two separated expansion theories (LE-2 or LE-3) for convergence reasons. The mathematical model adopted will be addressed as  $NB4 - 36LE T$  where  $N$  stands for the total number

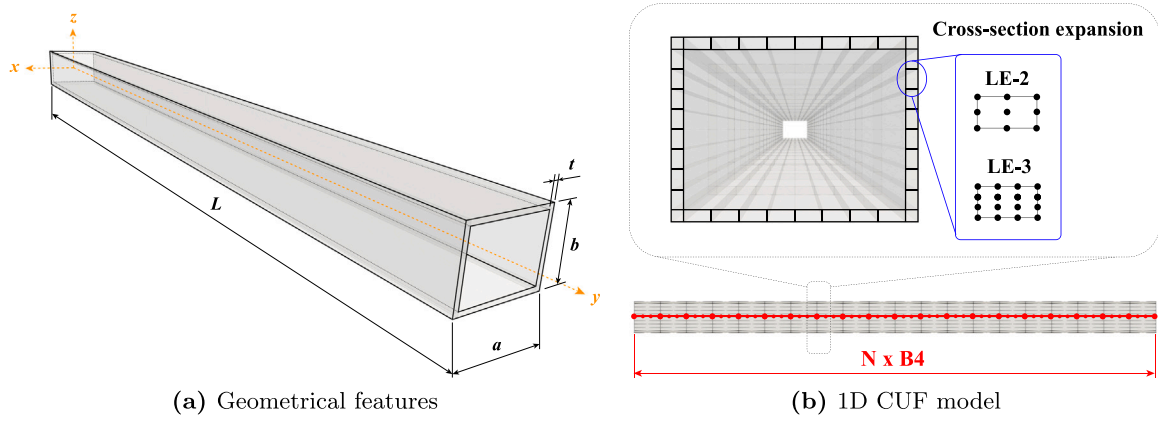


Fig. 19. Thin-walled box beam: geometrical features and discretization adopted.

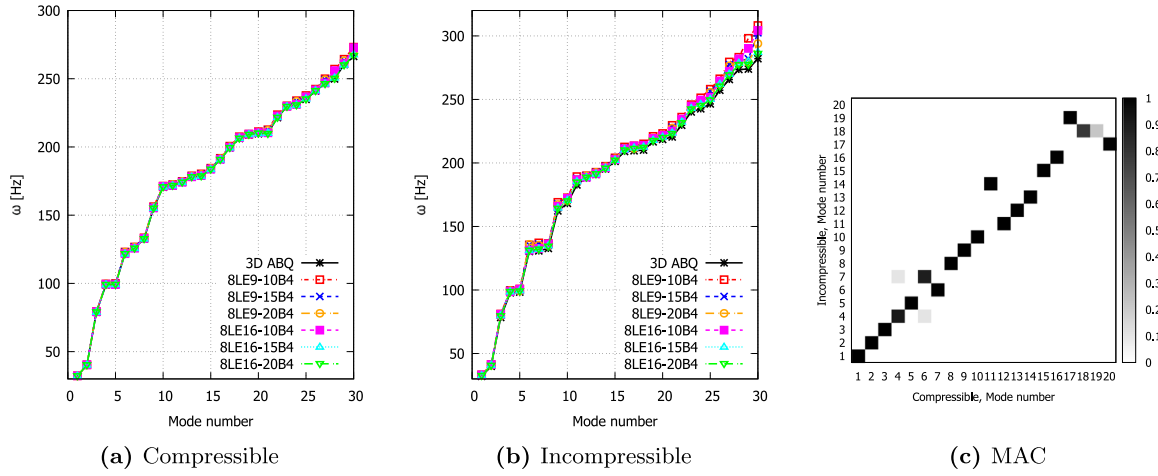


Fig. 20. Thin-walled box beam: MAC comparison between modes, clamped configuration.

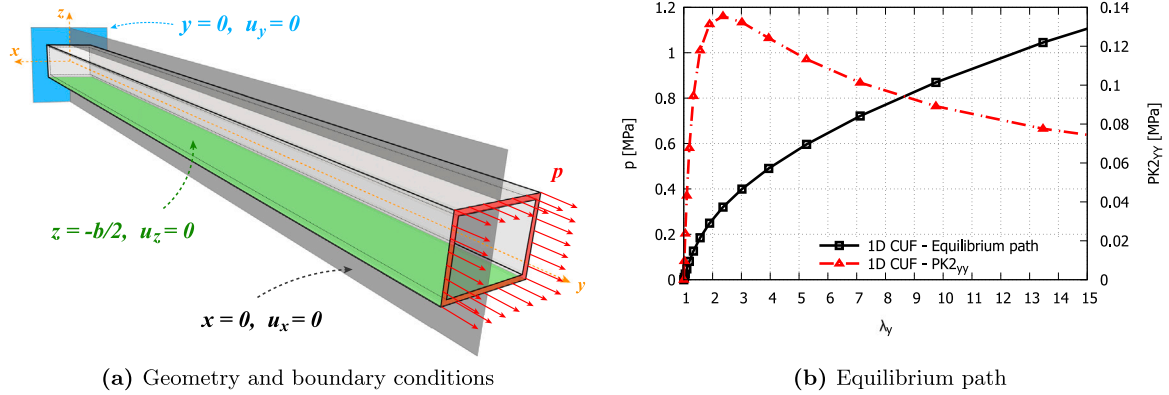


Fig. 21. Thin-walled box beam: equilibrium path for axial normal pressure.

of finite elements along the beam axis and  $T$  refers to the polynomial order of the cross-section expansion model. For each model, the total number of DOFs will be reported in the following.

In the first case, a convergence analysis for the free vibration problem around the trivial equilibrium state (undeformed configuration) is considered: natural frequencies are analyzed, both in the case of compressible and nearly-incompressible material, for different CUF discretizations. Tables 11 and 12 report the first five natural frequencies for the compressible and nearly-incompressible regime, comparing the total number of DOFs of each mathematical model adopted and the percentage difference between actual model results

and 3D ABAQUS reference. In the case of compressible material conditions, each model adopted is adequate for modal analysis and results are in excellent agreement with the reference. However, in the case of nearly-incompressible material, the need for higher-order theories is evident due to the limitation of a pure displacement-based finite element method in locking prevention, but the use of refined theories can mitigate these numerical effects. In both cases, saving in terms of computational costs required for the analysis can be observed. A wider spectrum of natural frequencies is depicted in Fig. 20(a) for the compressible case and Fig. 20(b) for the nearly-incompressible case, comparing the first thirty natural frequencies obtained adopting

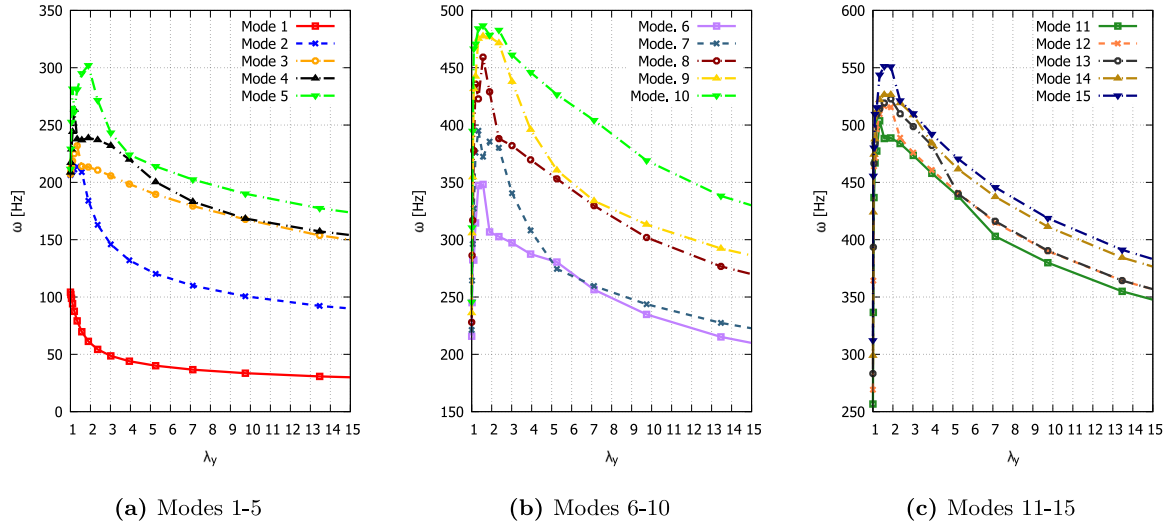


Fig. 22. Thin-walled box beam: natural frequencies versus traction pressure applied, compressible case.

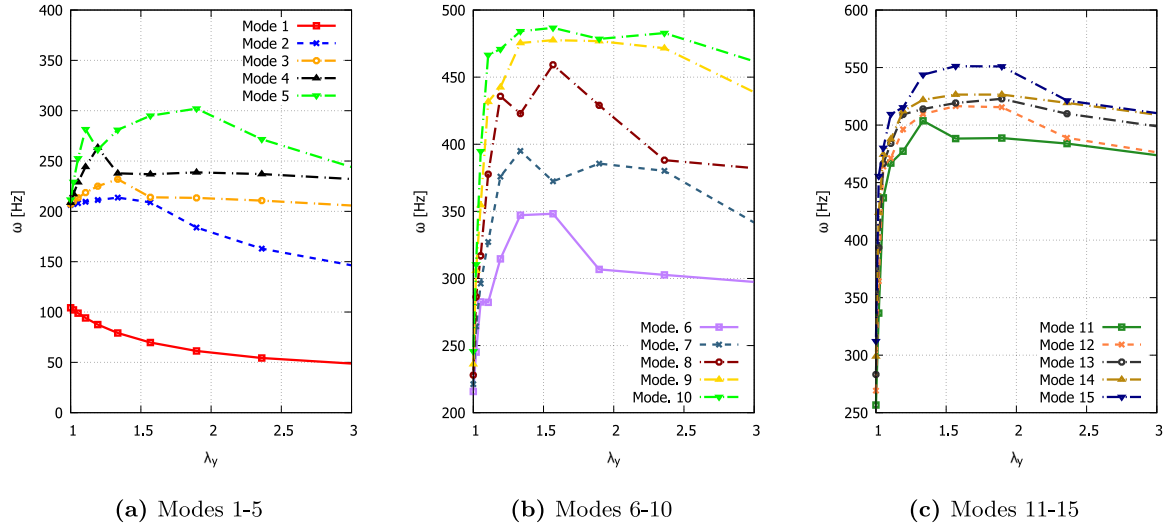


Fig. 23. Thin-walled box beam: natural frequencies versus traction pressure applied, compressible case.

Table 11

Thin-walled box beam: first five natural frequencies in the compressible regime [Hz].

Mode	36 LE-2 (parabolic model)			36 LE-3 (cubic model)			3D ABQ
	10B4	15B4	20B4	10B4	15B4	20B4	C8D20RH
1	32.28 <sup>(0.52%)</sup>	32.21 <sup>(0.32%)</sup>	32.18 <sup>(0.22%)</sup>	32.27 <sup>(0.48%)</sup>	32.20 <sup>(0.28%)</sup>	32.17 <sup>(0.18%)</sup>	32.11
2	40.37 <sup>(0.51%)</sup>	40.29 <sup>(0.31%)</sup>	40.25 <sup>(0.21%)</sup>	40.36 <sup>(0.49%)</sup>	40.28 <sup>(0.29%)</sup>	40.24 <sup>(0.19%)</sup>	40.16
3	79.33 <sup>(0.55%)</sup>	79.17 <sup>(0.35%)</sup>	79.10 <sup>(0.26%)</sup>	79.23 <sup>(0.42%)</sup>	79.07 <sup>(0.22%)</sup>	79.00 <sup>(0.14%)</sup>	78.90
4	99.54 <sup>(0.49%)</sup>	99.35 <sup>(0.29%)</sup>	99.86 <sup>(0.81%)</sup>	99.48 <sup>(0.43%)</sup>	99.15 <sup>(0.09%)</sup>	99.13 <sup>(0.08%)</sup>	99.06
5	99.92 <sup>(0.59%)</sup>	99.88 <sup>(0.54%)</sup>	99.26 <sup>(0.08%)</sup>	99.19 <sup>(0.15%)</sup>	99.29 <sup>(0.04%)</sup>	99.21 <sup>(0.13%)</sup>	99.34
DOFs	20088	29808	39528	40176	59616	79056	254118

refined models. As a final consideration, the normal modes of vibration of the compressible and nearly-incompressible case are compared by computing the MAC matrix considering eigenvectors associated with the 20B4-36LE-3 models, normal modes in different compressibility material conditions are compared to find possible correlations, and the final results are depicted in Fig. 20(c).

In the second case, the modal behavior of the compressible beam is investigated in non-trivial equilibrium conditions. Considering now a uniform normal pressure load applied at the tip-free end of the box beam, considering again the geometric boundary conditions for the uniaxial tension test shown in Fig. 21(a), a nonlinear static analysis is performed to obtain the equilibrium path and the stress distribution along the equilibrium curve, both showed in Fig. 21(b). Subsequently, in each

computed non-trivial equilibrium state, the free-vibration problem is solved. In this way, how natural frequencies and modal shapes are affected by the stretching ratio along the load direction can be investigated. Fig. 22 shows the variation of the first fifteen natural frequencies along the equilibrium path of the curve. Since there is a rapidly increasing stress value by looking at the equilibrium path, huge variations of the natural frequencies in the small/moderate strain regime are observed. The stretch-frequency curves in the small/moderate strain regime are depicted in Fig. 23 for the first fifteen modes. In general, a decreasing behavior of natural frequencies is observed since the principal stiffness term  $S_{yy}$  decreases during the load cycle, and mode aberration is observed. Finally, normal modes of vibration for the fixed value of stretch  $\lambda_y = 3.94$  are depicted in Fig. 24.

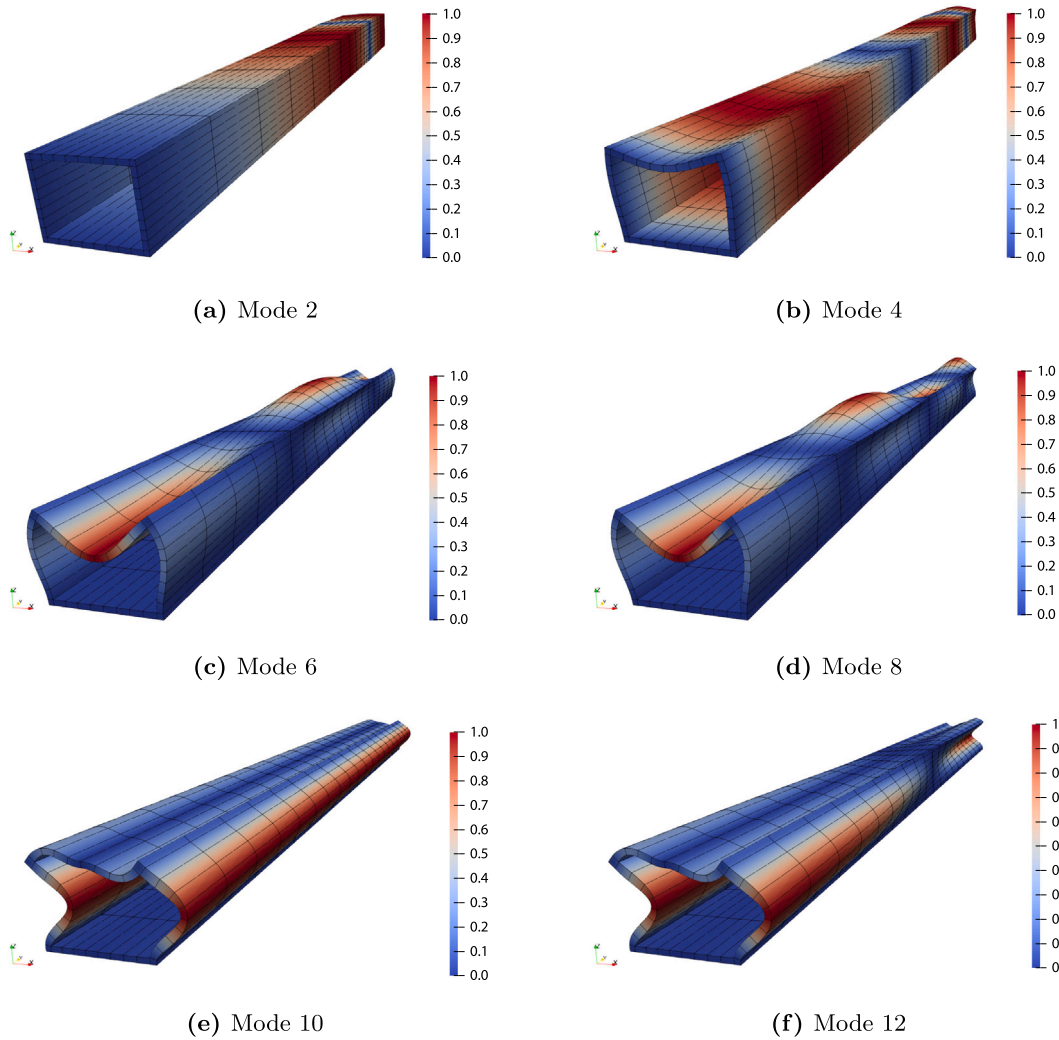


Fig. 24. Thin-walled box beam: normal modes of vibrations for  $\lambda_y = 3.94$ , eigenvector magnitude.

Table 12

Thin-walled box beam: first five natural frequencies in the nearly-incompressible regime [Hz].

Mode	36 LE-2 (parabolic model)			36 LE-3 (cubic model)			3D ABQ
	10B4	15B4	20B4	10B4	15B4	20B4	C8D20RH
1	33.21(3.70%)	32.78(2.34%)	32.57(1.70%)	33.19(3.63%)	32.76(2.27%)	32.55(1.63%)	32.03
2	41.35(3.54%)	40.83(2.23%)	40.59(1.62%)	41.34(3.50%)	40.82(2.19%)	40.57(1.57%)	39.94
3	81.09(3.43%)	80.16(2.24%)	79.71(1.67%)	80.90(3.19%)	79.97(2.01%)	79.53(1.44%)	78.40
4	99.59(1.84%)	99.49(1.74%)	99.19(1.44%)	98.80(1.04%)	98.70(0.94%)	98.65(0.89%)	97.79
5	100.77(2.44%)	99.70(1.36%)	99.44(1.09%)	100.67(2.34%)	99.60(1.26%)	99.09(0.74%)	98.36
DOFs	20088	29808	39528	40176	59616	79056	254118

## 6. Conclusions

In this paper, the unified 1D CUF beam finite element model for the vibration analysis of materials and structures is proposed, adopting the classical mathematical formulation of the undamped vibration problem and hyperelastic constitutive law written in terms of invariants of the deformation. In the CUF framework, nonlinear governing equations for the free vibration problem are written in a compact form, exploiting the independence of physical quantities involved from the kinematic expansion of the 3D displacement field, defined employing recursive index notation for arbitrary shape functions and expansion functions. The Principle of Virtual Displacement is written in matrix form deriving the analytic expression of mass matrix, tangent stiffness matrix, and internal and external forces vectors, defined in terms of fundamental

nuclei. The undamped vibration problem is then solved in trivial and non-trivial equilibrium states obtained from a static nonlinear analysis: the equilibrium path is obtained through a numerical scheme based on the Newton–Raphson iterative procedure coupled with the arc-length constraint.

The proposed results show the capabilities of refined fully nonlinear beam models to deal with the modal analysis of compressible and nearly-incompressible materials and structures, providing accurate results in terms of natural frequencies and modal behavior in trivial and non-trivial equilibrium states and description of local phenomena in the case of thin-walled structures. These kinds of investigations open to a wide range of analysis and further investigation in robotics, sensors, and measurement devices since it is possible to “tune” the modal behavior of the mechanical hyperelastic component by studying the appropriate pre-stressed condition.



Future works will deal with the extension of CUF hyperelastic models to the modal analysis of plates and shells structures, the generalization of undamped vibration problem for generic hyperelastic constitutive law (transversely isotropic or in-homogeneous anisotropic hyperelastic materials), investigating the effect of fiber-reinforcement and direction-dependent mechanical properties on the modal behavior of structures, and finally the analysis of the full dynamical behavior of soft structures including damping and viscosity constitutive behavior. Furthermore, implementation of locking correction techniques such as the *hybrid* formulation (or *u/p* formulation) and shear/membrane locking correction via Mixed Interpolation Tensorial Components are upcoming steps in the formulation of an efficient finite element model for nearly-incompressible hyperelasticity.

### CRedit authorship contribution statement

**A. Pagani:** Writing – review & editing, Supervision, Software, Resources, Methodology, Funding acquisition, Conceptualization. **P. Chiaia:** Writing – original draft, Visualization, Validation, Software, Methodology. **E. Carrera:** Writing – review & editing, Resources, Methodology, Funding acquisition, Conceptualization.

### Declaration of competing interest

The authors declare that they have no known competing financial interests or personal relationships that could have appeared to influence the work reported in this paper.

### Data availability

Data will be made available on request.

### References

- [1] A.N. Gent, A new constitutive relation for rubber, *Rubber Chem. Technol.* 69 (1) (1996) 59–61, <http://dx.doi.org/10.5254/1.3538357>.
- [2] A.N. Gent, Elastic instabilities in rubber, *Int. J. Non-Linear Mech.* 40 (2–3) (2005) 165–175, <http://dx.doi.org/10.1016/j.ijnonlinmec.2004.05.006>.
- [3] G.A. Holzapfel, T.C. Gasser, R.W. Ogden, A new constitutive framework for arterial wall mechanics and a comparative study of material models, *J. Elasticity* 61 (1/3) (2000) 1–48, <http://dx.doi.org/10.1023/a:1010835316564>.
- [4] R.W. Ogden, Large deformation isotropic elasticity – on the correlation of theory and experiment for incompressible rubberlike solids, *Proc. R. Soc. Lond. Ser. A Math. Phys. Eng. Sci.* 326 (1567) (1972) 565–584, <http://dx.doi.org/10.1098/rspa.1972.0026>.
- [5] I. Breslavsky, M. Amabili, M. Legrand, Static and dynamic behavior of circular cylindrical shell made of hyperelastic arterial material, *J. Appl. Mech.* 83 (5) (2016) <http://dx.doi.org/10.1115/1.4032549>.
- [6] M. Amabili, P. Balasubramanian, I.D. Breslavsky, G. Ferrari, R. Garziera, K. Riabova, Experimental and numerical study on vibrations and static deflection of a thin hyperelastic plate, *J. Sound Vib.* 385 (2016) 81–92, <http://dx.doi.org/10.1016/j.jsv.2016.09.015>.
- [7] H.B. Khaniki, M.H. Ghayesh, R. Chin, M. Amabili, A review on the nonlinear dynamics of hyperelastic structures, *Nonlinear Dynam.* 110 (2) (2022) 963–994, <http://dx.doi.org/10.1007/s11071-022-07700-3>.
- [8] M. Amabili, Nonlinear damping in large-amplitude vibrations: Modelling and experiments, *Nonlinear Dynam.* 93 (1) (2017) 5–18, <http://dx.doi.org/10.1007/s11071-017-3889-z>.
- [9] D.C. Pamplona, P.B. Gonçalves, S.R.X. Lopes, Finite deformations of cylindrical membrane under internal pressure, *Int. J. Mech. Sci.* 48 (6) (2006) 683–696, <http://dx.doi.org/10.1016/j.ijmecsci.2005.12.007>.
- [10] I.D. Breslavsky, M. Amabili, M. Legrand, Physically and geometrically non-linear vibrations of thin rectangular plates, *Int. J. Non-Linear Mech.* 58 (2014) 30–40, <http://dx.doi.org/10.1016/j.ijnonlinmec.2013.08.009>.
- [11] I.D. Breslavsky, M. Amabili, M. Legrand, Nonlinear vibrations of thin hyperelastic plates, *J. Sound Vib.* 333 (19) (2014) 4668–4681, <http://dx.doi.org/10.1016/j.jsv.2014.04.028>.
- [12] R.M. Soares, P.B. Gonçalves, Large-amplitude nonlinear vibrations of a Mooney–Rivlin rectangular membrane, *J. Sound Vib.* 333 (13) (2014) 2920–2935, <http://dx.doi.org/10.1016/j.jsv.2014.02.007>.
- [13] P. Balasubramanian, G. Ferrari, M. Amabili, Z.J.G.N. del Prado, Experimental and theoretical study on large amplitude vibrations of clamped rubber plates, *Int. J. Non-Linear Mech.* 94 (2017) 36–45, <http://dx.doi.org/10.1016/j.ijnonlinmec.2016.12.006>.
- [14] M.S. Arani, M. Bakhtiari, A.A. Lakis, Analyzing softening and hardening behavior in vibration of a thin incompressible hyperelastic cylindrical shell, *Thin-Walled Struct.* 189 (2023) 110943, <http://dx.doi.org/10.1016/j.tws.2023.110943>.
- [15] R. Azzara, E. Carrera, M. Filippi, A. Pagani, Time response stress analysis of solid and reinforced thin-walled structures by component-wise models, *Int. J. Struct. Stab. Dyn.* 20 (14) (2020) 2043010, <http://dx.doi.org/10.1142/s0219455420430105>.
- [16] E. Carrera, A.G. de Miguel, A. Pagani, Component-wise analysis of laminated structures by hierarchical refined models with mapping features and enhanced accuracy at layer to fiber-matrix scales, *Mech. Adv. Mater. Struct.* 25 (14) (2017) 1224–1238, <http://dx.doi.org/10.1080/15376494.2017.1396631>.
- [17] E. Carrera, A. Pagani, S. Valvano, Multilayered plate elements accounting for refined theories and node-dependent kinematics, *Composites B* 114 (2017) 189–210, <http://dx.doi.org/10.1016/j.compositesb.2017.01.022>.
- [18] A. Pagani, R. Augello, E. Carrera, Frequency and mode change in the large deflection and post-buckling of compact and thin-walled beams, *J. Sound Vib.* 432 (2018) 88–104, <http://dx.doi.org/10.1016/j.jsv.2018.06.024>.
- [19] E. Carrera, A. Pagani, R. Augello, Vibration of metallic and composite shells in geometrical nonlinear equilibrium states, *Thin-Walled Struct.* 157 (2020) 107131, <http://dx.doi.org/10.1016/j.tws.2020.107131>.
- [20] A. Pagani, E. Carrera, Unified one-dimensional finite element for the analysis of hyperelastic soft materials and structures, *Mech. Adv. Mater. Struct.* (2021) 1–14, <http://dx.doi.org/10.1080/15376494.2021.2013585>.
- [21] R. Augello, E. Carrera, M. Filippi, A. Pagani, E. Tortorelli, Unified plate finite elements for the large strain analysis of hyperelastic material structures, *Int. J. Non-Linear Mech.* (2023) 104465, <http://dx.doi.org/10.1016/j.ijnonlinmec.2023.104465>.
- [22] A. Pagani, P. Chiaia, M. Filippi, M. Cinefra, Unified three-dimensional finite elements for large strain analysis of compressible and nearly incompressible solids, *Mech. Adv. Mater. Struct.* (2023) 1–21, <http://dx.doi.org/10.1080/15376494.2023.2229832>.
- [23] P.J. Flory, Thermodynamic relations for high elastic materials, *Trans. Faraday Soc.* 57 (1961) 829, <http://dx.doi.org/10.1039/tf9615700829>.
- [24] T. Sussman, K.J. Bathe, A finite element formulation for nonlinear incompressible elastic and inelastic analysis, *Comput. Struct.* 26 (1–2) (1987) 357–409, [http://dx.doi.org/10.1016/0045-7949\(87\)90265-3](http://dx.doi.org/10.1016/0045-7949(87)90265-3).
- [25] I. Castañar, J. Baiges, R. Codina, A stabilized mixed finite element approximation for incompressible finite strain solid dynamics using a total Lagrangian formulation, *Comput. Methods Appl. Mech. Engrg.* 368 (2020) 113164, <http://dx.doi.org/10.1016/j.cma.2020.113164>.
- [26] G.A. Holzapfel, *Nonlinear Solid Mechanics*, Wiley, 2000, p. 455.
- [27] E. Carrera, G. Giunta, M. Petrolo, *Beam Structures Classical and Advanced Theories*, Wiley, Chichester, West Sussex, UK, 2011, p. 208.
- [28] A. Pagani, E. Carrera, Unified formulation of geometrically nonlinear refined beam theories, *Mech. Adv. Mater. Struct.* 25 (1) (2016) 15–31, <http://dx.doi.org/10.1080/15376494.2016.1232458>.
- [29] A.R. Sánchez-Majano, R. Azzara, A. Pagani, E. Carrera, Accurate stress analysis of variable angle tow shells by high-order equivalent-single-layer and layer-wise finite element models, *Materials* 14 (21) (2021) 6486, <http://dx.doi.org/10.3390/ma14216486>.
- [30] A. Pagani, R. Azzara, R. Augello, E. Carrera, Stress states in highly flexible thin-walled composite structures by unified shell model, *AIAA J.* 59 (10) (2021) 4243–4256, <http://dx.doi.org/10.2514/1.j060024>.
- [31] E. Carrera, M. Petrolo, Refined one-dimensional formulations for laminated structure analysis, *AIAA J.* 50 (1) (2012) 176–189, <http://dx.doi.org/10.2514/1.j051219>.
- [32] B. Wu, A. Pagani, M. Filippi, W.Q. Chen, E. Carrera, Accurate stress fields of post-buckled laminated composite beams accounting for various kinematics, *Int. J. Non-Linear Mech.* 111 (2019) 60–71, <http://dx.doi.org/10.1016/j.ijnonlinmec.2019.02.002>.
- [33] E. Carrera, A. Pagani, M. Petrolo, E. Zappino, Recent developments on refined theories for beams with applications, *Mech. Eng. Rev.* 2 (2) (2015) 14–00298–14–00298, <http://dx.doi.org/10.1299/mer.14-00298>.
- [34] E. Carrera, M. Cinefra, E. Zappino, M. Petrolo, *Finite Element Analysis of Structures Through Unified Formulation*, Wiley, 2014, <http://dx.doi.org/10.1002/9781118536643>.
- [35] M.A. Crisfield, An arc-length method including line searches and accelerations, *Internat. J. Numer. Methods Engrg.* 19 (9) (1983) 1269–1289, <http://dx.doi.org/10.1002/nme.1620190902>.
- [36] E. Carrera, A study on arc-length-type methods and their operation failures illustrated by a simple model, *Comput. Struct.* 50 (2) (1994) 217–229, [http://dx.doi.org/10.1016/0045-7949\(94\)90297-6](http://dx.doi.org/10.1016/0045-7949(94)90297-6).